IS-T--1525

DE91 012677

Nuclear Magnetic Resonance Studies of Atomic Motion in Lithium Chloroborate and Lithium Thiosilicate Glassy Fast Ionic Conductors

by

Trunnell, Mark

MS Thesis submitted to Iowa State University

Ames Laboratory, U.S. DOE
Iowa State University
Ames, Iowa 50011

Date Transmitted: May 14, 1991

PREPARED FOR THE U.S. DEPARTMENT OF ENERGY
UNDER CONTRACT NO. W-7405-Eng-82.

AVAILABILITY:

To DOE and DOE contractors: Office of Scientific and Technical Information
P.O. Box 62
Oak Ridge, TN 37831

prices available from: (615) 576-8401
FTS: 626-8401

To the public: National Technical Information Service
U.S. Department of Commerce
5285 Port Royal Road
Springfield, VA 22161

TABLE OF CONTENTS

LIST OF FIGURES

LIST OF TABLES

I. INTRODUCTION

The energy crisis of the early 1970s spurred great interest in the development of alternate energy sources and of particular interest was the development of automobiles that could be powered by electricity. These would require fuel cells that could deliver large currents for extended periods of time in order to provide the consumers with their desired performance. The potential of fast ionic and superionic conductors as electrolytic materials was immediately seen and the interest in these materials grew. Although the great interest in electric cars has faded in the past two decades the interest in glassy fast ionic and superionic conductors both in the areas of fuel cell technology and as a basic physical system has continued to grow.

The microscopic mechanisms responsible for the high conductivity of these glasses which may be greater than $10^{-4}(\Omega\ \mathrm{cm})^{-1}$ at room temperature[1] is still not well understood; NMR provides a tool to study the motion of the ions on a microscopic scale.[2]

In this work two such fast ionic conductors are examined: lithium chloroborate glass (B_2O_3+Li_2O+LiCl) and lithium thiosilicate glass (Li_2S+SiS_2). A review of the basic NMR theory that is relevant to these systems will be presented first. This will be presented in two parts; the first where the theories relevant to the NMR spectra are discusses and the second where spin lattice relaxation is examined.

In the next section, some of the general properties of alkali borate and alkali thiosilicate glasses are discussed. The structures present in the borate and thiosilicate glasses[3-19] will be reviewed first showing the different boron and silicon sites within each. This section will conclude with an examination of d.c. conductivity measurements[20-29] of both alkali borate and alkali thiosilicate glasses and an examination of a.c. conductivity measurements of on lithium thiosilicate sample used for the NMR measurements along with a derivation of the frequency dependent conductivity starting from the electric modulus.[30-33]

In section IV the preparation techniques, instrumentation and experimental methods used will be discussed and the NMR data that was collected on the samples will be presented.

In Section V the experimental results will be discussed. The lithium chloroborate glass is examined first by examining the ^{11}B spectra and showing that the results obtained here are consistent with those obtained by Bray and others.[8-15] The ^7Li nuclear spin lattice relaxation is examined next and showing that the BPP[34] theory does not accurately describe the temperature and frequency dependence but if the KWW[35-37] form of the correlation function is used, the measurements can be accurately described. Next the ^{11}B nuclear spin lattice relaxation is examined and it is shown that it agrees well with the theory proposed by Rubenstein and Resing[38,39] which uses a two phonon Raman process for the relaxation. It is also shown here that there is some evidence of coupling between the ^{11}B relaxation and the lithium diffusional motion. This has been observed in various silver chloroborate glasses.[40,41]

Section V is concluded by looking at the results of the ^{7}Li nuclear spin lattice relaxation in the lithium thiosilicate glass. Here again it is found that the BPP[34] theory does not accurately describe both the temperature and frequency dependence but by using the KWW[35-37] form of the correlation an accurate description of the relaxation can be achieved. It is argued in the conclusions whether the KWW form of the correlation function indicates the presence of a distribution of activation energies or collective effects in the ionic motion or both. The fact that the a.c conductivity data can also be described by the same correlation function but with different parameters causes one to favor the second hypothesis.

II. REVIEW OF NMR THEORY

In this section, the theories that are relevant to the work done for this thesis will be reviewed using both quantum and classical arguments and will be specific for the nuclei studied. The relevant physical data for these nuclei are shown[42] in Table 1.

A. Classical NMR Description[43,44]

A nucleus with spin $I > 0$ has a nuclear magnetic dipole moment $\vec{\mu} = \gamma\hbar\vec{I}$, where γ is the gyromagnetic ratio of the nucleus. For a macroscopic sample made up of a large number of individual moments, the net magnetization $\vec{M}$ is given by

$$\vec{M} = \sum_i \vec{\mu_i} \quad . \tag{1}$$

In the absence of an external magnetic field, the orientations of the individual magnetic moments are random resulting in $\vec{M} = 0$.

If a nucleus is placed in a magnetic field $\vec{H} = H_0\hat{z}$ the following equation of motion is obtained:

$$\frac{d\vec{\mu}}{dt} = \gamma\vec{\mu} \times \vec{H} \tag{2}$$

If the equation of motion is transformed into a reference frame (x',y',z') which is centred on the nucleus and rotating with angular velocity $\vec{\omega}$ where $\vec{\omega}$ is antiparallel to $\vec{H}$, then

$$\frac{d\vec{\mu}}{dt} = \gamma\vec{\mu} \times \vec{H}_{eff} \tag{3}$$

where

$$\vec{H}_{eff} = \vec{H} + \frac{\vec{\omega}}{\gamma} \tag{4}$$

In this rotating frame, the magnetic dipole moment has no time dependence if $\vec{\omega}$ is chosen such that $\vec{H}_{eff} = 0$ resulting in $\omega = \gamma H_0 \equiv \omega_0$. This is known as the Larmor condition and ω_0 as the Larmor frequency.

If a time varying magnetic field in the laboratory frame of the form

$$\vec{H} = H_0\hat{z} + H_1[\cos(\omega t)\hat{x} + \sin(\omega t)\hat{y}] \tag{5}$$

is applied, $\vec{H}_{eff}$ becomes

$$\vec{H}_{eff} = \vec{H}_0 + \frac{\vec{\omega}}{\gamma} + \vec{H}_1 \tag{6}$$

The coordinate system in the rotating frame (x', y', z') is defined such that $\vec{H} = H_0\hat{z}'$ and $\vec{H}_1 = H_1\hat{y}'$ resulting in $\vec{H}_{eff}$ having the orientation shown in Figure 1 and the magnitude of $\vec{H}_{eff}$ being given by

$$H_{eff} = \sqrt{\left(H_0 + \frac{\omega}{\gamma}\right)^2 + H_1^2}\ . \tag{7}$$

In the rotating frame, the individual magnetic moments processes about $\vec{H}_{eff}$ with an angular frequency $\omega_{eff} = \gamma H_{eff}$.

H_0 is typically several orders of magnitude larger than H_1 resulting in $\vec{H}_{eff}$ and therefore the net magnetization to remain essentially parallel to $\vec{H}_0$ for most values of $\vec{\omega}$ but at the Larmor frequency $\vec{H}_{eff} = \vec{H}_1$. At this frequency, the net magnetization which was initially in the z' direction now precesses about $\vec{H}_1$ at a frequency $\omega_{eff} = \gamma H_1$ and it remains in the x'-z' plane. This is called being on resonance.

B. NMR Spectra for a Rigid Lattice

The magnetization can be rotated to any angle with respect to H_0 by simply varying the time H_1 is applied when at resonance. To rotate the magnetic moment through 90°, a pulse of time $t_{90} = \frac{\pi/2}{\gamma H_{eff}}$ is applied. Similarly, the moment can be rotated through an angle of 180° by using a pulse of length $t_{180} = 2t_{90} = \frac{\pi}{\gamma H_{eff}}$.

If a single nucleus is placed in a magnetic field H_0 and given a 90° pulse, classically its magnetic moment would be left rotating in the x-y plane with a frequency of ω_0 for an infinite amount of time. If a solenoid were placed with its axis both in the X-Y plane and on the nucleus, the induced voltage would be of the form $A\sin(\omega_0 t)$ and the Fourier transform would be a δ-function centred at ω_0.

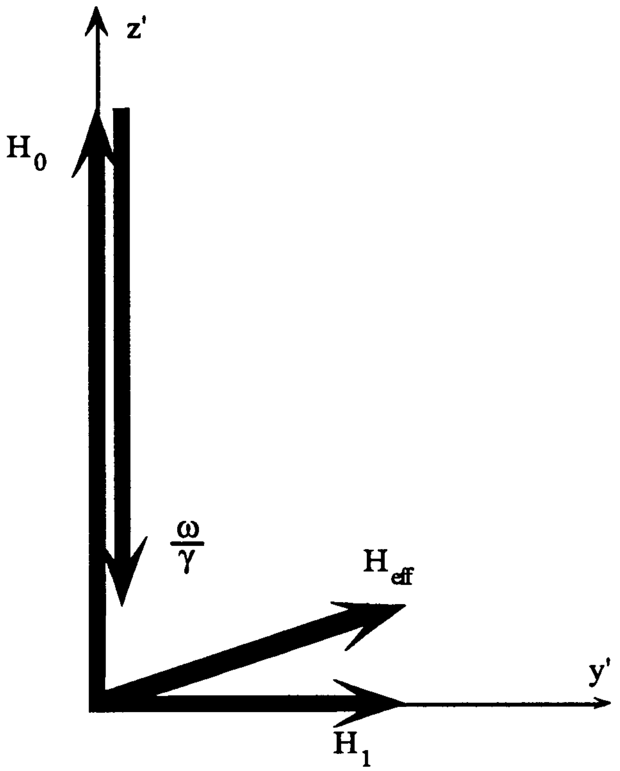

Figure 1. Vector diagram showing $\vec{H}_{eff}$ in rotating frame

Table 1. Properties of ^{7}Li and ^{11}B Nuclei

Nucleus	^{7}Li	^{11}B
Spin (I)	3/2	3/2
Gyromagnetic Ratio $\left(\frac{\gamma}{2\pi}\right)$	16.547 MHz/T	13.660 MHz/T
Magnetic Moment (μ)	3.2560 μ_N	2.6880 μ_N
Electric Quadrupole Moment (eQ)	-0.1 barn	0.0355 barn

In an actual sample, there are on the order of 10^{22} individual nuclei present and each is interacting with its environment through a variety of mechanisms. Some of these may include interactions of the nuclear magnetic moment with the surrounding lattice, with other nuclear magnetic moments or with inhomogeneities in the magnetic field, or interactions of the nuclear quadrupole moment, if it has one, with any electric field gradients that may be present.

If any of these mechanisms are present, the magnetization in the X-Y plane will decay in time as[45] $M_0 e^{-t/T_2^*}$ where M_0 is the initial magnetization and T_2^* is the decay constant. The magnetization as a function of time is shown in Figure 2a. The value of T_2^* can be determined from the envelope of the oscillating magnetization or from the Fourier transform as shown in Figure 2b. These mechanisms each have the effect of broadening the NMR line from the ideal δ-function.

1. Inhomogeneous broadening[45]

The line broadening mechanisms can be broken into several categories. Inhomogeneous broadening is an examined first. This type of broadening comes about from the fact that each nucleus does not have the same chemical environment. In an amorphous or glassy material, different local fields can be due to the fact that the distance between each nucleus and its nearest neighbors is somewhat random while in a crystalline material local inhomogeneous fields can be due to imperfections or impurities within the lattice. It can also be due to the external magnetic field H_0 not being uniform in space. As a result, there is a spread in the magnetic field at the different sites and each nucleus precesses at a slightly different rate.

If a 90° pulse was given, at time $t = 0$ the magnetization would lie in the x' direction as shown in Figure 3a. As time progresses, some nuclei are precessing faster and some slower so the individual magnetic moments begin to fan out as seen in Figure 3b and Figure 3c. After many times T_2^* has passed, the individual moments point uniformly in all directions and the net magnetization is zero.

2. Homogeneous broadening

The second type of broadening is homogeneous broadening and will be described here by using the theory of moments first introduced by J. H. Van Vleck[46] in 1948.

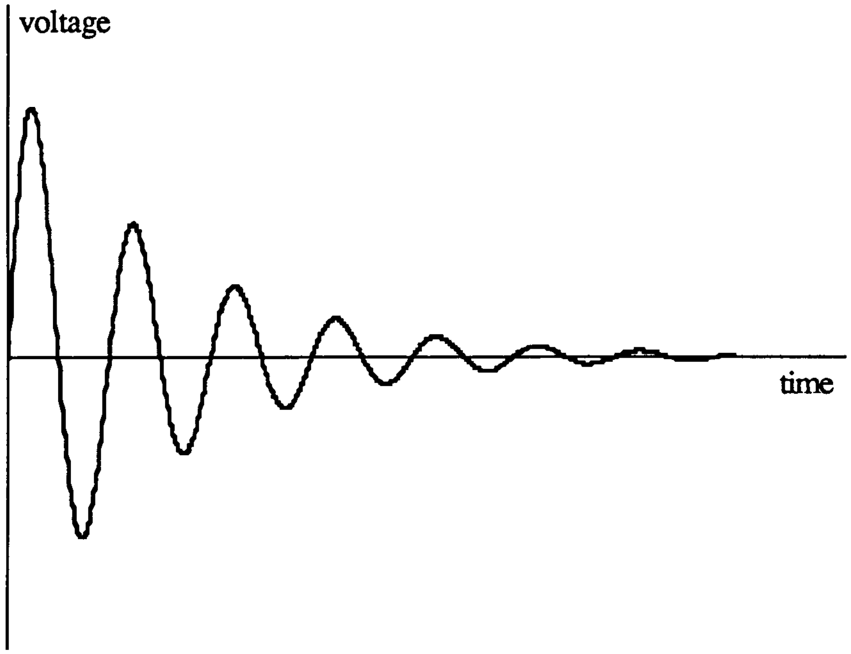

Figure 2a. Free induction decay signal with decay time T_2^*

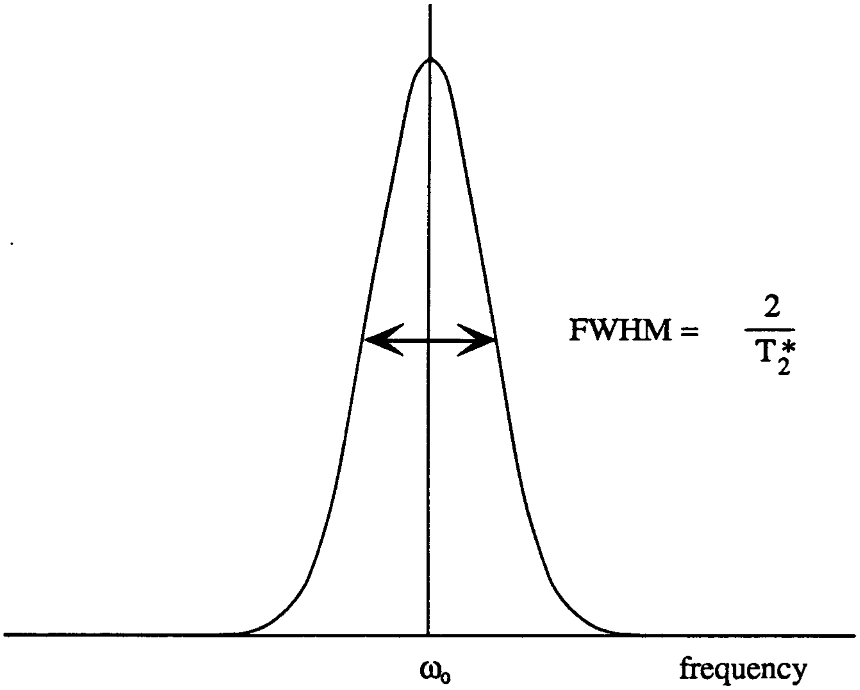

Figure 2b. Fourier transform of free induction decay

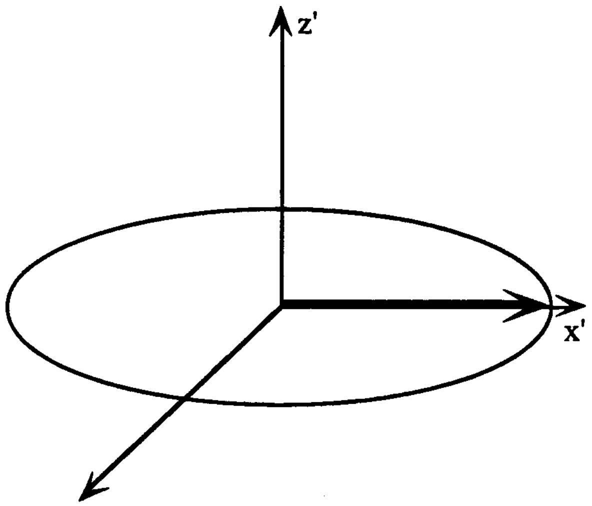

Figure 3a.
Magnetic moments at time $t = 0$

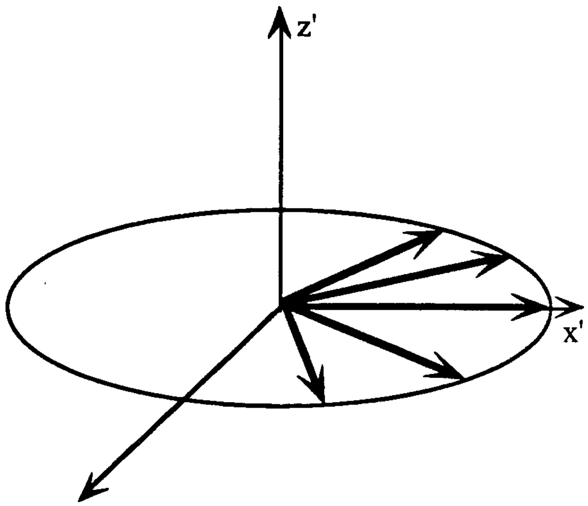

Figure 3b.
Magnetic moments at time $0 < t < T_2^*$

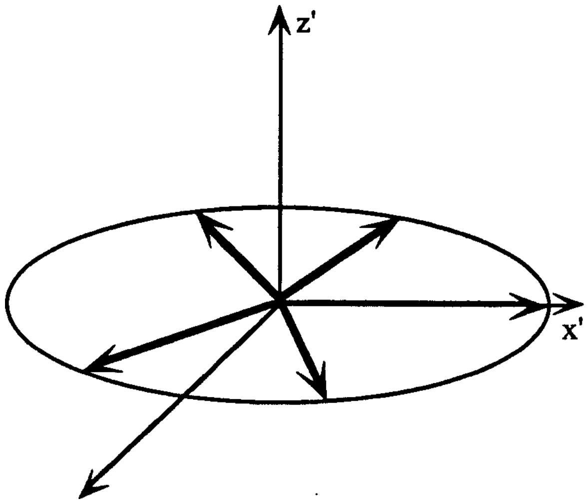

Figure 3c.
Magnetic moments at time $t \approx T_2^*$

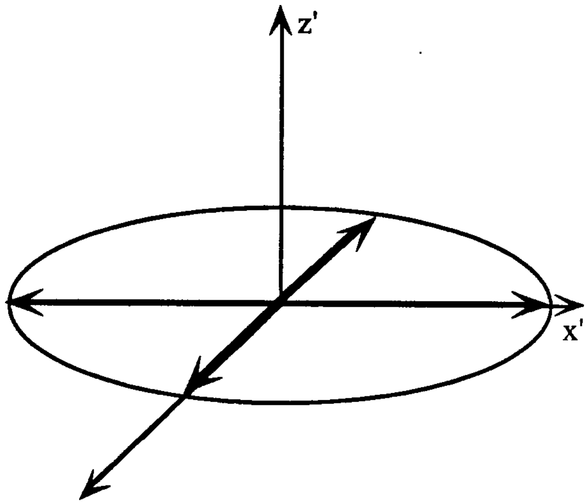

Figure 3d.
Magnetic moments at time $t \gg T_2^*$

If the nucleus has a non zero spin, then it has a magnetic dipole moment $\mu = \gamma\hbar I$. The interaction of this magnetic dipole with a magnetic field $\vec{H}_0 = H_0\hat{z}$ gives the Hamiltonian

$$\mathcal{H}_z = -\hbar\gamma H_0 I_z \qquad (8)$$

which yields the Zeeman energy eigenstates $E = -mh\gamma H_0$. This results in a splitting of the degenerate energy levels into 2I+1 evenly spaced levels. The frequency of the transition between the m and m-1 levels is ν_0 where $\nu_0 = \gamma H_0$. This splitting is shown schematically in Figure 4 for a spin $\frac{3}{2}$ nucleus.

For a system of spins in a magnetic field the Hamiltonian can be written as[47]

$$\hbar\mathcal{H} = \hbar(\mathcal{H}_z + \mathcal{H}_1) \qquad (9)$$

where $\mathcal{H}_z$ gives the Zeeman splitting due to the field and $\mathcal{H}_1$ is the magnetic dipole-dipole interaction resulting in

$$h\mathcal{H} = -\gamma h H_0 \sum_j I_z + h^2\gamma^2 \sum_{j<k} \frac{1}{r_{jk}^3}\left\{\vec{I}_j\cdot\vec{I}_k - 3\frac{(\vec{I}_j\cdot\vec{r}_{jk})(\vec{I}_k\cdot\vec{r}_{jk})}{r_{jk}^2}\right\}. \qquad (10)$$

This can be approximated as

$$h\mathcal{H} = -\gamma h H_0 \sum_j I_z + h^2\gamma^2 \sum_{j<k} \frac{I_{zj}I_{zk}\left(1-3\cos^2\theta\right) + \tfrac{1}{2}\left(1-3\cos^2\theta\right)\left(I_{zj}I_{zk} - \vec{I}_j\cdot\vec{I}_k\right)}{r_{jk}^3} \qquad (11)$$

where θ is the angle of r with respect to H_0.

The dipole dipole interaction has the effect of making the 2I+1 Zeeman levels spaced slightly differently for each nucleus. Solving this exactly for 10^{22} individual spins is nearly impossible, therefore some other method must be used. A common method of studying the line shape is the use of moments. The nth moment can be defined as

$$S_n = \frac{\int_0^\infty (x-x_0)^n f(x)dx}{\int_0^\infty f(x)dx} \qquad (12)$$

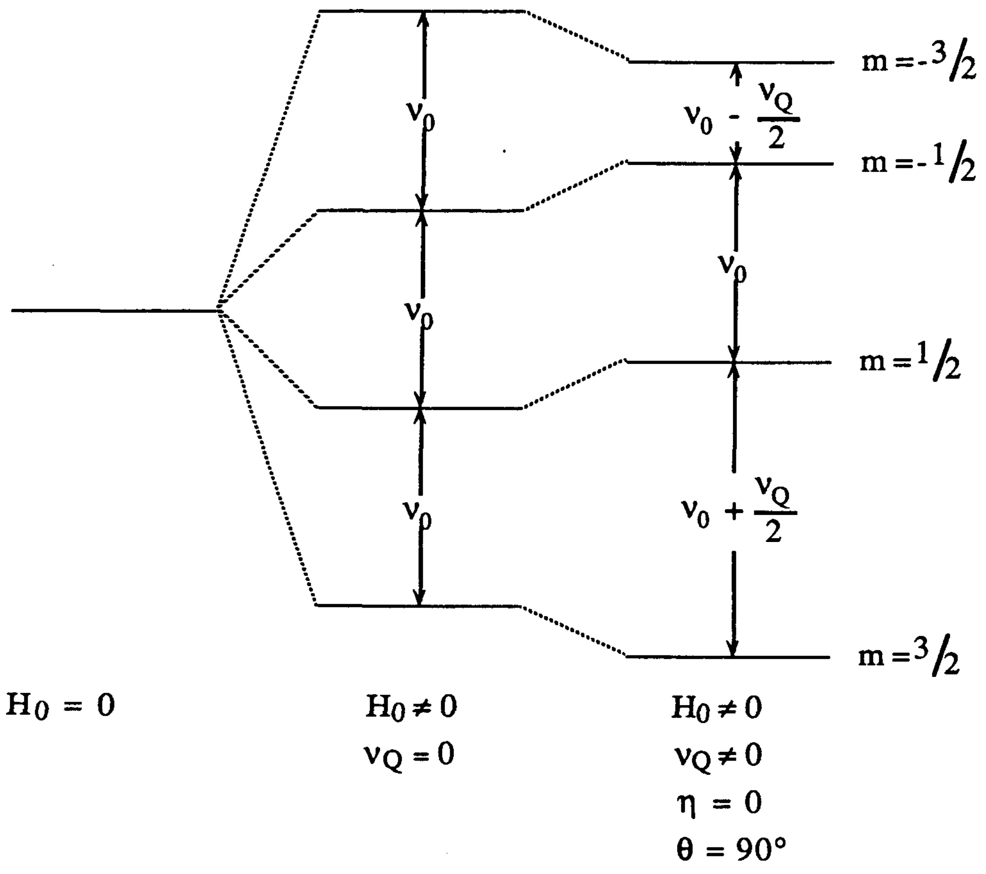

Figure 4. Energy level diagram for $I = \frac{3}{2}$

where x is either frequency or field and f(x) is the function describing the shape of the spectrum. If f(x) is an even function, the odd moments all vanish.

The most commonly used functions for f(x) are the Gausian and the Lorentzian given by[45]

$$f(x) = \frac{1}{\sigma\sqrt{2\pi}} \exp\left[- \frac{(x-x_0)^2}{2\sigma^2} \right] \tag{13}$$

and

$$f(x) = \frac{1}{\pi T_2} \frac{1}{\left(1/T_2\right)^2 + (x-x_0)^2} \tag{14}$$

respectively.

If f(x) is chosen to be a Gausian, it is found that[45] $S_2 = \sigma^2$, $S_4 = 3\sigma^4$ and $S_{2n} = 1\cdot 3\cdot 5\cdot \ldots \cdot (2n-1)\ \sigma^{2n}$ and the full width at half maximum is 2.36σ. If f(x) is chosen to be a Lorentzian, the integrals do not converge and another technique must be used.

One possible way to treat this is to cut the Lorentzian off at some point where it becomes too small to be measured and evaluate the resulting integrals. This method tends to introduce large errors into the values of the higher moments.

Another technique is to use the free induction decay f(t). If f(t) is expanded in a Taylor series, the result is

$$f(t) = M_0 \left(1 - S_2 \frac{t^2}{2!} + S_4 \frac{t^4}{4!} - S_6 \frac{t^6}{6!} + \cdots \right). \tag{15}$$

Using the formula for the coefficients of a Taylor series the moments can be determined.

The contribution of the spins themselves to the second moment is now considered. If the spins of the nucleus under inspection and its neighbors are the same, it can be shown that[46]

$$S_{2\,II} = \frac{3}{4} \gamma^4 \hbar^2 I(I+1) \sum_k \frac{\left(1-3\cos^2\theta_{kj}\right)^2}{r_{kj}^6} \tag{16}$$

For a powder or an amorphous sample, the contribution of θ_{kj} can be determined and gives[47]

$$S_{2\,II} = \frac{3}{5}\gamma^4 \hbar^2 I(I+1) \sum_k \frac{1}{r_{kj}^6} \tag{17}$$

If however there are different spins I and S, it can be shown that[45]

$$S_{2\,IS} = \frac{4}{15}\gamma_I^2 \gamma_S^2 \hbar^2 S(S+1) \sum_k \frac{1}{r_{kj}^6} \tag{18}$$

where S represents the neighbor and I the nucleus under inspection.

3. Effects of electric quadrupole interactions

In addition to the magnetic dipole-dipole interactions, a nucleus with spin $I>\frac{1}{2}$ also has an electric quadrupole moment which can interact with an electric field gradient (EFG). The interaction of this quadrupole moment with an electric field gradient is described by the Hamiltonian[48,49]

$$\mathcal{H}_Q = \frac{h\nu_Q}{6}\left[3I_z^2 - I^2 + \eta\left(I_x^2 - I_y^2\right)\right] \tag{19}$$

where

$$\nu_Q = \frac{3e^2qQ}{2I(2I-1)h} \tag{20}$$

and

$$\eta = \frac{V_{xx} - V_{yy}}{V_{zz}} \tag{21}$$

and where $q = V_{zz}$ is the maximum component of the EFG tensor in its principle axis system (x,y,z), and η is the asymmetry parameter.

If $\mathcal{H} = \mathcal{H}_Z + \mathcal{H}_Q$ and $\mathcal{H}_Q$ is treated as a perturbation, the Hamiltonian can be solved using Rayleigh-Schrödinger perturbation theory. Solving to first order gives

$$E_m = -mh\nu_0 + \frac{h\nu_Q}{12}\left[3m^2 - I(I+1)\right]\Theta \tag{22}$$

where

$$\Theta = 3\cos^2\theta - 1 + \eta\cos 2\varphi\left(\cos^2\theta - 1\right) \tag{23}$$

and where θ and φ are the angles formed by the electric field gradient with the laboratory reference frame (X,Y,Z). The frequencies of the transitions between m and m-1 for $I = \frac{3}{2}$ become

$$\begin{gathered}\nu_{3/2\leftrightarrow 1/2} = \nu_0 - \frac{\nu_Q}{2}\Theta \\ \nu_{1/2\leftrightarrow -1/2} = \nu_0 \\ \nu_{-1/2\leftrightarrow -3/2} = \nu_0 + \frac{\nu_Q}{2}\Theta\end{gathered} \tag{24}$$

These transitions are shown schematically in Figure 4 for $\eta = 0$ and $\theta = 90°$.

Sometimes it is necessary to use a sample that is not a single crystal. In the case of metals, skin depth effects limit the penetration of the RF field to a few microns so that fine polycrystalline powders must be used. Another case is that of noncrystalline, amorphous or glassy materials. In these materials the principle axis system and therefore the angles θ and φ can vary from site to site resulting in a continuous distribution of frequencies over a wide spectral range.

In the case of the $m = \frac{1}{2}$ to $\frac{3}{2}$ transition with $\eta = 0$, the spread of the transition frequency is from $\nu_0 - \frac{\nu_Q}{2}$ for $\theta = 90°$ to $\nu_0 + \nu_Q$ for $\theta = 0°$. The intensity of the spectrum is not however constant over this range since there are many more sites with their EFG principle axis pointing at 90° than there are pointing at 0° with reference to the applied field H_0. The intensity distribution for $\eta = 0$ can be found by assuming $I(\nu)d\nu = \sin\theta d\theta$ and $\nu = \nu_0 + \nu_Q(3\cos^2\theta - 1)/2$ resulting in

$$I(\nu) \propto \frac{1}{\sqrt{2x+1}} \tag{25}$$

where $x = \frac{(\nu - \nu_0)}{\nu_Q}$ and $-\frac{1}{2} < x < 1$. The $m = -\frac{3}{2}$ to $-\frac{1}{2}$ transition yields the same results except the spectrum is transposed about ν_0. The $m = -\frac{1}{2}$ to $\frac{1}{2}$ transitions are not affected to first order and therefore no angular dependence of the line is present. The resulting polycrystalline pattern is shown in Figure 5a.

Actual polycrystalline spectra are smoothed out by dipolar broadening. This results in spectra similar to that shown in Figure 5b. The major features of these are the large central peak at ν_0, the two smaller satellite peaks at $\nu_0 \pm \frac{\nu_Q}{2}$ and the shoulders at $\nu_0 \pm \nu_Q$. As can be easily seen, the spacing between the satellites is ν_Q and the spacing between the shoulders is $2\nu_Q$.

If the Hamiltonian is now solved to second order for $I = \frac{3}{2}$ and for an axially symmetric EFG, the frequency transitions obtained are:[48]

$$\nu(m \leftrightarrow m-1) = \nu_0 + \tfrac{1}{2}\nu_Q(m - \tfrac{1}{2})\left(3\cos^2\theta - 1\right) + \frac{\nu_Q^2}{32\nu_0}\left(1 - \cos^2\theta\right)\left\{\left[102m(m-1) - \frac{57}{2}\right]\cos^2\theta - \left[6m(m-1) - \frac{9}{2}\right]\right\} \qquad (26)$$

Solving to second order has no effect on the position of the satellites but does produce a splitting in the central peak. This splitting comes from the last term which gives[48]

$$\nu(-\tfrac{1}{2} \rightarrow \tfrac{1}{2}) = \nu_0 + \frac{3\nu_Q^2}{32\nu_0}\left(1 - \cos^2\theta\right)\left(1 - 9\cos^2\theta\right) \qquad (27)$$

Looking again at a polycrystalline sample, singularities in intensity for $\theta = 41.81°$ and $\theta = 90°$ and a small shoulder for $\theta = 0°$ are obtained. The polycrystalline spectrum for the central peak is shown in Figure 6a.[47]

The frequencies corresponding to these singularities are[48]

$$\nu^{I} = \nu_0 + \frac{3\nu_Q^2}{16\nu_0} \qquad (28)$$

$$\nu^{II} = \nu_0 - \frac{\nu_Q^2}{3\nu_0} \qquad (29)$$

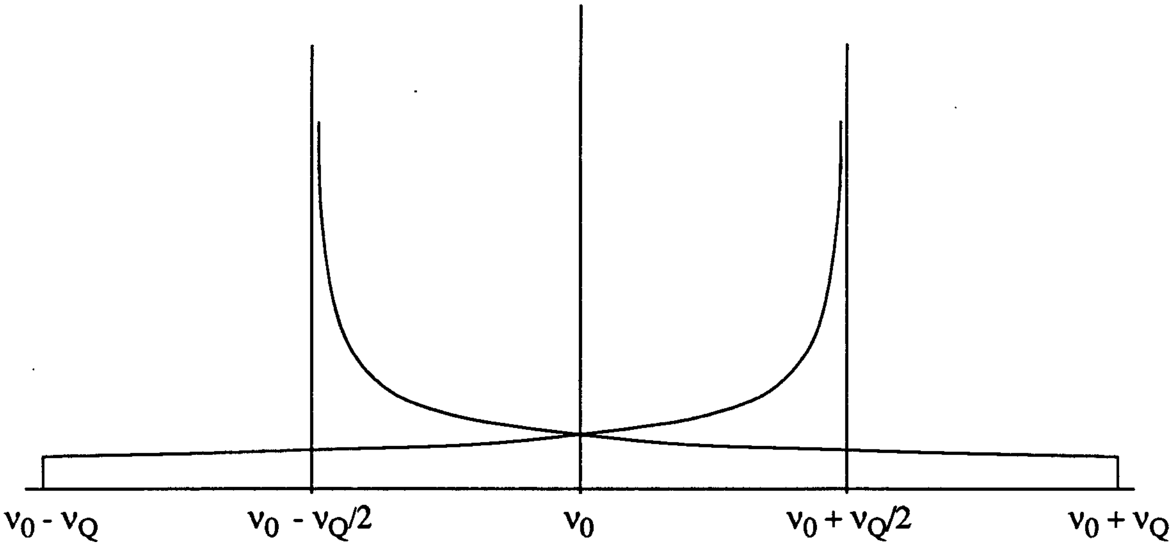

Figure 5a. First order quadrupole spectrum for a polycrystalline sample $I = \frac{3}{2}$, $\eta = 0$

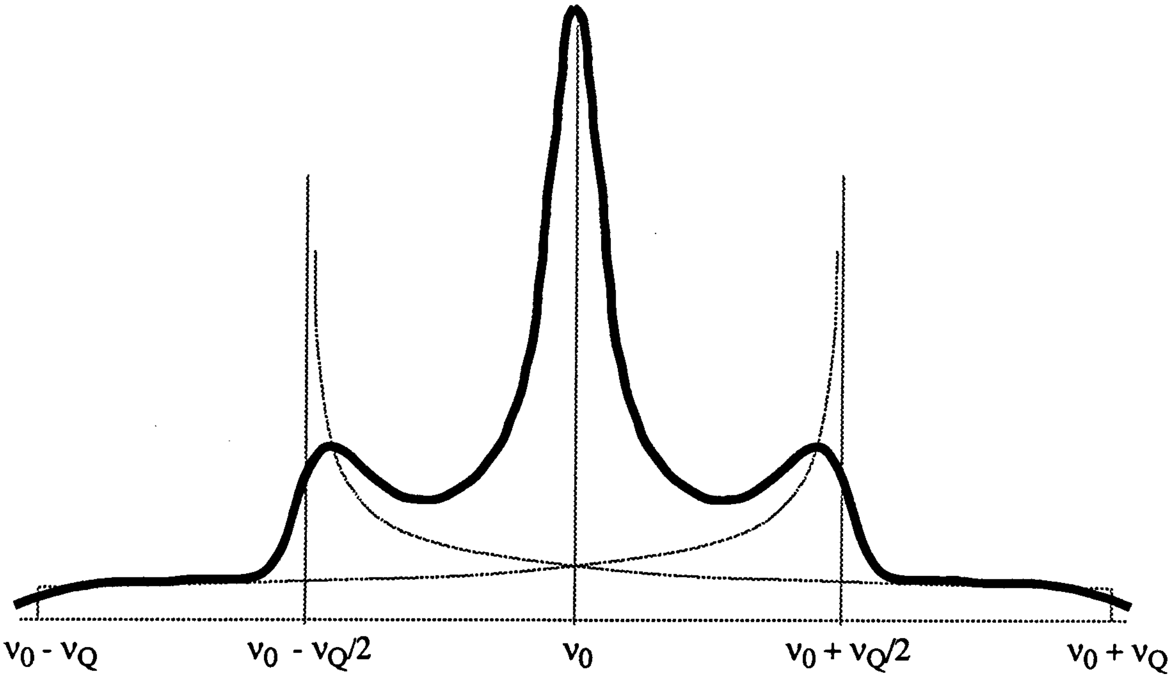

Figure 5b. First order quadrupole spectrum with dipolar broadening

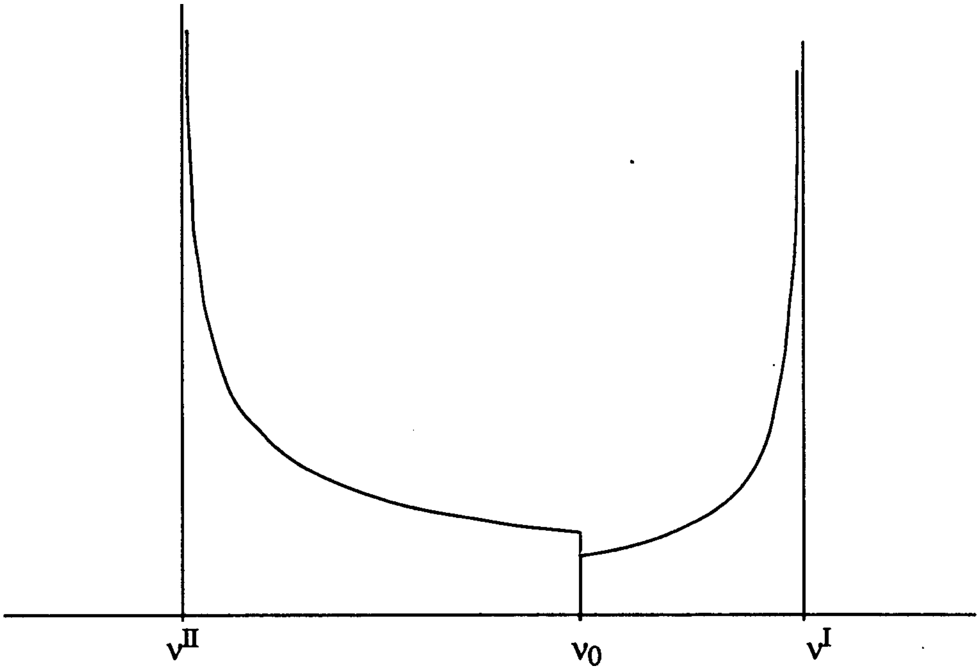

Figure 6a. Second order quadrupole spectrum of central peak for polycrystaline sample for $I = \frac{3}{2}$, $\eta = 0$

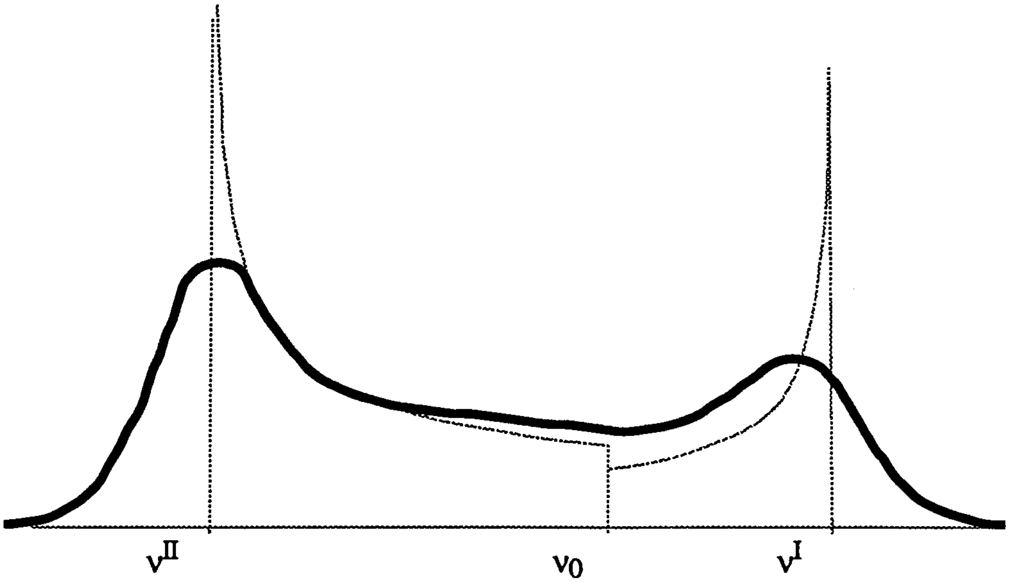

Figure 6b. Second order quadrupole spectrum with dipolar broadening

and if $\Delta\nu = \nu^{I} - \nu^{II}$[48]

$$\Delta\nu = \frac{25\nu_Q^2}{48\nu_0}. \tag{30}$$

Thus, from the second order quadrupole perturbed NMR spectrum (Figure 6b), an independent measure of ν_Q can be obtained and compared with the one obtained from the splitting of the satellite transitions. It should be noted that second order splitting $\Delta\nu$ is inversely proportional to ν_0, this being important in establishing the origin of the observed spectrum.

C. Spin Lattice Relaxation

If a sample which initially had no net magnetization is placed it in a magnetic field, the Zeeman levels would split and momentarily the number of spins occupying each level would be the same. After some time elapsed, the spins would redistribute themselves until they were in their equilibrium distribution given by the Boltzmann's distribution and a net magnetization would be formed. The magnetization would grow as[45] $M_0(1 - e^{-t/T_1})$ where the time constant T_1 is called the spin lattice relaxation time and M_0 is the saturation magnetization. T_1 is often as short as a few milliseconds but as stated earlier, spontaneous emission between Zeeman levels is exceedingly small therefore there must be some other mechanism that allows the spins to relax quickly.

1. Master equation for $I = \frac{3}{2}$

As shown previously (see Figure 4), if a system of spin I is placed in a magnetic field H, the energy levels split into 2I + 1 separate Zeeman levels. At equilibrium, the population of these levels is given by the Boltzmann's equation and therefore the rate at which nuclei leave a given level must be equal to the rate at which they arrive at that level. This results in[47]

$$\frac{dN_n}{dt} = \sum_m \left(N_m W_{mn} - N_n W_{nm}\right) \tag{31}$$

where N_n is the population of the n^{th} level and W_{mn} is transition probability from the m^{th} state to the n^{th} state and is called the master equation.

If it is assumed that the spin lattice relaxation mechanism is predominantly magnetic as is the case for ^{7}Li in the samples studied here, the transitions between Zeeman levels are restricted to those where $\Delta m = \pm 1$ only. It can then be shown that[50]

$$W_{m\rightarrow m+1} = W_M(I+m)(I-m+1) \tag{32}$$

where W_M is the relaxation transition probability due to the coupling of the nuclear magnetic moment with the degrees of freedom of the lattice. For $I = \frac{3}{2}$, the probabilities become[50]

$$W_{3/2\rightarrow 1/2} = W_{-1/2\rightarrow -3/2} = 3W_M \tag{33}$$

and

$$W_{1/2\rightarrow -1/2} = 4W_M. \tag{34}$$

If $N_{m+1} - N_m \equiv N_{m+\frac{1}{2}}$ and $N_p' \equiv N_p - n_0$ where n_0 is the difference in population between adjacent levels when equilibrium between the system and lattice is achieved with no RF power, it can be shown that[50]

$$\dot{N}_1' = -6N_1'W_M + 4N_0'W_M \tag{35}$$

$$\dot{N}_0' = 3N_1'W_M - 8N_0'W_M - 3N_{-1}'W_M \tag{36}$$

$$\dot{N}_{-1}' = 4N_0'W_M - 6N_{-1}'W_M \tag{37}$$

Solving this system of three equations gives[50]

$$\frac{N_1' - n_0}{n_0} = a_1 e^{-2W_N t} + a_2 e^{-6W_N t} + a_3 e^{-12\,W_N t} \tag{38}$$

where a_1, a_2 and a_3 are determined by initial conditions.

If it is assumed that the Zeeman levels are equally spaced and the levels are completely saturated, a_2 and a_3 both become zero and the above equation reduces to

$$\frac{N_1' - n_0}{n_0} = a_1 e^{-t/T_1} \tag{39}$$

where $\frac{1}{T_1} = 2W_M$. This T_1 is the same spin lattice relaxation time mentioned earlier.

If the Zeeman levels are not equally spaced, there are many different possible results. Three special cases are examined here. The first occurs if the spacings are not too different so that all levels can be saturated. If this is the case the same results are obtained as above with a single exponential decay and a T_1 given by $\frac{1}{T_1} = 2W_M$.

If the spacings are spread enough to allow saturation the central transition with a single short 90° pulse without affecting the population of the higher and lower energy levels, the result is

$$\frac{N_1' - n_0}{n_0} = E_1\left(0.1e^{-2W_N t} + 0.9e^{-12W_N t}\right). \tag{40}$$

For this case there is no single decay time so a single T_1 can not be defined.

The last case holds if the spacings are spread enough to allow only the central transition to be saturated but the higher and lower energy levels are allowed to come to equilibrium with the central levels by using a series of 90° pulses for a time longer than T_1, one obtains

$$\frac{N_1' - n_0}{n_0} = E_1\left(0.4e^{-2W_N t} + 0.6e^{-12W_N t}\right). \tag{41}$$

Again, there is no single decay time so a single T_1 can not be defined here either.

If the relaxation mechanism is controlled by quadrupole interactions as is the case for ^{11}B, then two relaxation transition probabilities W_1 and W_2 corresponding to transitions between Zeeman levels with $\Delta m = \pm 1$ and $\Delta m = \pm 2$ respectively can be defined. In the case of quadrupole relaxation the solution of the master equation is more difficult and an analytic solution exists for only a few special cases[51]. For $I = \frac{3}{2}$ and equally spaced Zeeman levels one gets

$$\frac{N'_1 - n_0}{n_0} = E_1 e^{-2/5(W_1+4W_2)t} \tag{42}$$

and for saturation of the central line only one gets

$$\frac{N'_1 - n_0}{n_0} = E_1\left(\frac{1}{2}e^{-2W_1t} + \frac{1}{2}e^{-2W_2t}\right). \qquad (43)$$

If $W_1 = W_2 = W_Q$ as is the case in many polycrystalline or amorphous samples, $\frac{1}{T_1} = 2W_Q$.

2. Relation of spectral density to T_1

As stated earlier, if a spin system is to relax its Zeeman levels must couple with the energy modes within the surrounding lattice. A mechanism for this relaxation is now examined.

The nuclei within a solid can interact with each other through dipole-dipole interactions, they can interact with EFGs through quadrupole interactions or they can interact with the magnetic moments of electrons of other ions within the solid. Whenever any of these processes are modulated in time, transitions between Zeeman levels can occur. In the previous section, it was stated that $\frac{1}{T_1} = 2W_M$ (or W_Q) where W_M is the probability of a transition occurring. If there are many modes within the the lattice with frequency ω_0 available, then W_M is large and T_1 is short. If however, there are few modes with frequency ω_0, W_M will be small and T_1 long.

For the spin Hamiltonian written as[52]

$$\hbar\mathcal{H} = \hbar\mathcal{H}_0 + \hbar\mathcal{H}(t) \qquad (44)$$

where $\mathcal{H}_0$ represents the time independent interactions with the lattice and external field and $\mathcal{H}(t)$ and time dependent interactions, the probability of a transition occurring between the m^{th} and the $m\text{-}1^{th}$ levels is given to first order by[52]

$$W_{m,m-1} = \int_0^t \langle m-1|\mathcal{H}^*|m\rangle\langle m|\mathcal{H}|m-1\rangle e^{i\omega_0(t-t')}\,dt' \qquad (45)$$

If $\mathcal{H}(t)$ is random, then taking a statistical average gives[52]

$$W_{m,m-1} = \int_0^t G_1(t'-t)\ e^{i\omega_0(t-t')}dt' \tag{46}$$

where $G_1(t'-t)$ is the correlation function for $\langle m|\mathcal{H}'|m-1\rangle$. If $G_1(t'-t)$ is dependent only upon $t' - t = \tau$, then

$$W_{m,m-1} = \int_{-t}^t G_1(\tau)\ e^{i\omega_0 t}dt \quad . \tag{47}$$

For times greater than the time of the transition itself,

$$W_{m,m-1} = \int_{-\infty}^{\infty} G_1(\tau)\ e^{i\omega_0 t}\, d\tau \propto J(\omega_0) \quad . \tag{48}$$

For dipole-dipole interactions, it can be shown by either time dependent perturbation theory or by using the density matrix that[34]

$$\frac{1}{T_1} = A\left[J^{(1)}(\omega_0) + J^{(2)}(2\omega_0)\right] \tag{49}$$

where $J^{(1)}$ corresponds to an interaction with one spin flip and $J^{(2)}$ corresponds to an interaction with two spin flips. It can also be shown that $J^{(2)} = 4J^{(1)} \equiv J$ resulting in

$$\frac{1}{T_1} = A\left[J(\omega_0) + 4J(2\omega_0)\right] \quad . \tag{50}$$

From these equations T_1 can be calculated from knowing the form of the spectral density.

3. BPP theory

One of the most successful theories of nuclear magnetic relaxation is that proposed by Bloembergen, Purcell and Pound (BPP).[34] The BPP theory, which applies best to liquids, assumes that the motions of the spins within the sample are purely random. This gives a form of the correlation as follows:

$$G_1(t) = \overline{\mathcal{H}^2(t)}\, e^{-t/\tau_c} \tag{51}$$

where τ_c is the correlation time and is a measure of the time it takes for a given interaction to change significantly. In many cases, it can be written as

$$\tau_c = \tau_0 e^{E_a/k_B T} \tag{52}$$

where τ_0 is the prefactor, E_a is the activation energy, k_B is Boltzmann's constant and T is the absolute temperature. Putting this into the form for $W_{m,m-1}$ gives

$$W_{m,m-1} = \frac{1}{2T_1} = A\left[\frac{\tau_c}{1+\omega^2\tau_c^2} + \frac{4\tau_c}{1+4\omega^2\tau_c^2}\right]. \tag{53}$$

A plot of $W_{m,m-1}$ versus frequency for various temperatures is shown in Figure 7a.

Instead of holding the temperature fixed and measuring $W_{m,m-1}$ for various temperatures, what is usually done is to hold the frequency fixed and measure T_1 for various temperatures. This gives results similar to that shown in Figure 7b. Note that Figure 7b actually shows $\ln(T_1)$ vs. 1/temperature as it is typically plotted.

Many features of the BPP theory can be determined from this figure. First of all, at high temperatures, T_1 is independent of frequency. This can be shown by taking the limit as T gets very large and the ω dependence falls out. When data is plotted in this way, the slope of the data to the left of the minimum is proportional to E_a. This allows a simple method of determining the activation energy.

The values of the various temperature minima, T_{min}, lie in a straight line and occur when $\omega\tau_c \approx 0.64$. From this and from the values of E_a and ω the value of the prefactor τ_0 can be determined.

On the low temperature side of the curve the slope is the same as that on the high temperature except for a sign change. This is one of the key differences between data that follows the BPP theory and that which does not.

4. <u>Stretched exponential correlation function</u>

The BPP theory does not work well in all cases, one in particular being fast ionic conductors. As stated above, the BPP theory assumes that each jump in position of the

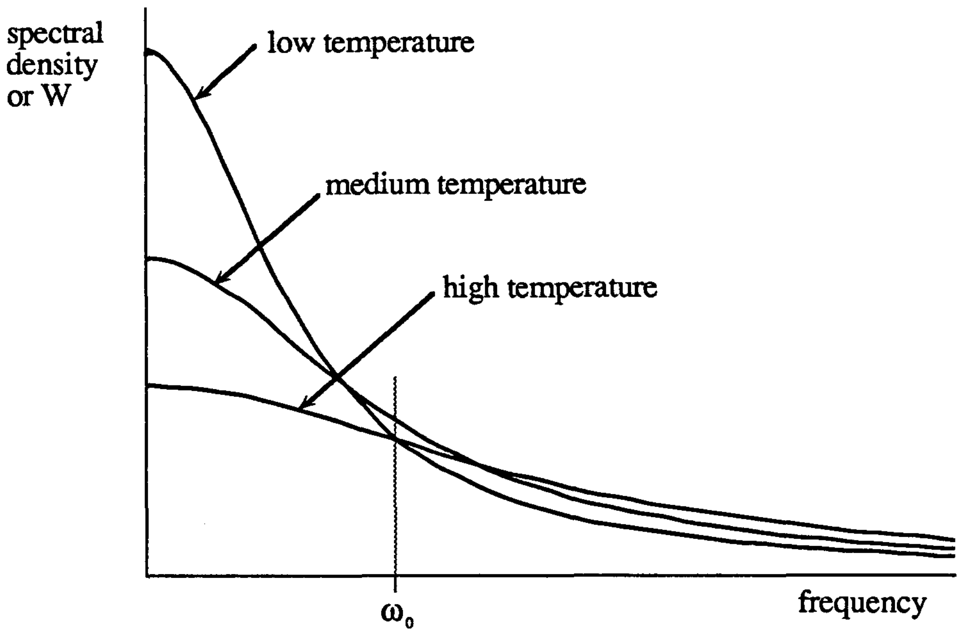

Figure 7a. Spectral density of a lattice versus frequency for different temperatures

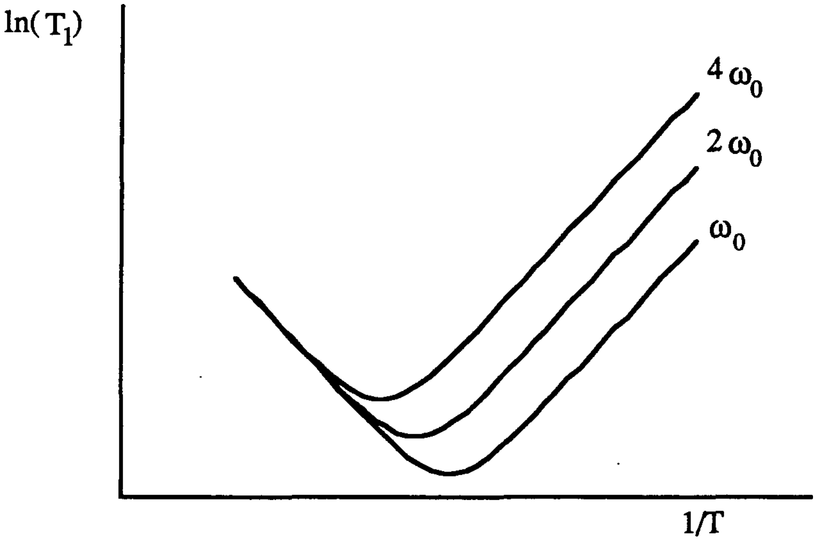

Figure 7b. $\ln(T_1)$ versus 1/T for different frequencies

spins is purely random. In many compounds, it seems that the probability that the ion will jump back to where it was is greater than the probability that it will jump anywhere else. The result of this is that the correlation function is no longer a simple exponential but rather a stretched exponential which has the form[35-37]

$$G_1(t) = \overline{\mathcal{H}^2(t)}\, e^{-\left(t/\tau_c\right)^{\beta}} \tag{54}$$

where $0 \leq \beta \leq 1$. This correlation function has been given the name KWW after Kohlrausch[36,37] who used it in 1854 and later by Williams and Watts[35] who rediscovered it in 1970. The stretched exponential can be viewed as the result of a distribution of correlation times $\rho(t)$ given by

$$e^{-\left(t/\tau_c\right)^{\beta}} = \int \rho(\tau)\, e^{-t/\tau}\, d\tau \quad . \tag{55}$$

Note that the BPP theory is simply the special case of $\rho(t) = \delta(\tau-\tau_c)$ resulting in $\beta = 1$.

This leads to the problem that

$$J(\omega) = \int_{-\infty}^{\infty} G_1(t)\, e^{i\omega_0 t}\, dt = 2\int_{0}^{\infty} \cos(\omega_0 t)\, e^{-\left(t/\tau_c\right)^{\beta}}\, dt \tag{56}$$

has no known analytic solution except for the special cases of β being an integer or $\omega\tau_c = 0$. In order to make use of this the integral must be solved numerically (see Appendix A).

III. GENERAL PROPERTIES OF BORATE AND THIOSILICATE GLASSES

In this section some of the general properties of alkali borate and alkali thiosilicate glasses will be examined as well as some of the previous work that has been done on them. In particular the structure of the glasses and the conductivity measurements done will be examined.

A. Structure of B_2O_3+Li_2O Glass

The structures of B_2O_3+Li_2O and other alkali borate glasses have been studied in great detail. Much work has been done using infra-red and X-ray spectroscopy [3-7] where it was found that the alkali borate glasses are made up of seven basic units; orthoborate, pyroborate, metaborate, diborate, boroxol, tetraborate and loose BO_4 each of which is shown in Figure 8.

NMR studies have shown which of these basic units are present and in what concentrations.[8-14] Since ^{10}B and ^{11}B both are spin $I > \frac{1}{2}$, they each have an electric quadrupole moment that can interact with any local electric field gradients (EFGs) that may be present. If a boron nucleus is sitting at the center of four oxygen nuclei where the oxygen forms a tetrahedron, the EFG at the site of the boron is very small due to the symmetry of the oxygen, but if the boron sits at the center of only three oxygen nuclei, the oxygen can only form a triangle and there is no longer any symmetry out of the plane of the oxygen and large EFGs and possible at the boron site. NMR allows a method of measuring the fraction of the boron nuclei in the BO_4 sites and the fraction in the BO_3 sites, these are known as N_4 and N_3 respectively. This is done by measuring the relative strength of the signals that come from nuclei that do not lie in an EFG to those that do lie in an EFG.

N_4 has been measured[8] for $xR_2O+(1-x)B_2O_3$ where R is an alkali metal. For $x = 0$, $N_4 \approx 0.04$ but as x increases, N_4 also increases until $x \approx 0.35$ where $N_4 \approx 0.45$. N_4 remains fairly constant until $x \approx 0.45$, then N_4 decreases back to $N_4 \approx 0$ at $x \approx 0.7$. The identity of the alkali metal used seems to have no effect on the structure of the glass. For the samples used here, R is Li and $x = 0.41$ resulting in $N_4 \approx 0.45$.

It has been demonstrated[15] that B_2O_3+Ag_2O glass is structurally the same as the alkali borate glasses and measurements of N_4 yield similar values. There are also similarities in the values of the quadrupole coupling coefficient of ^{11}B reported for the silver borate and

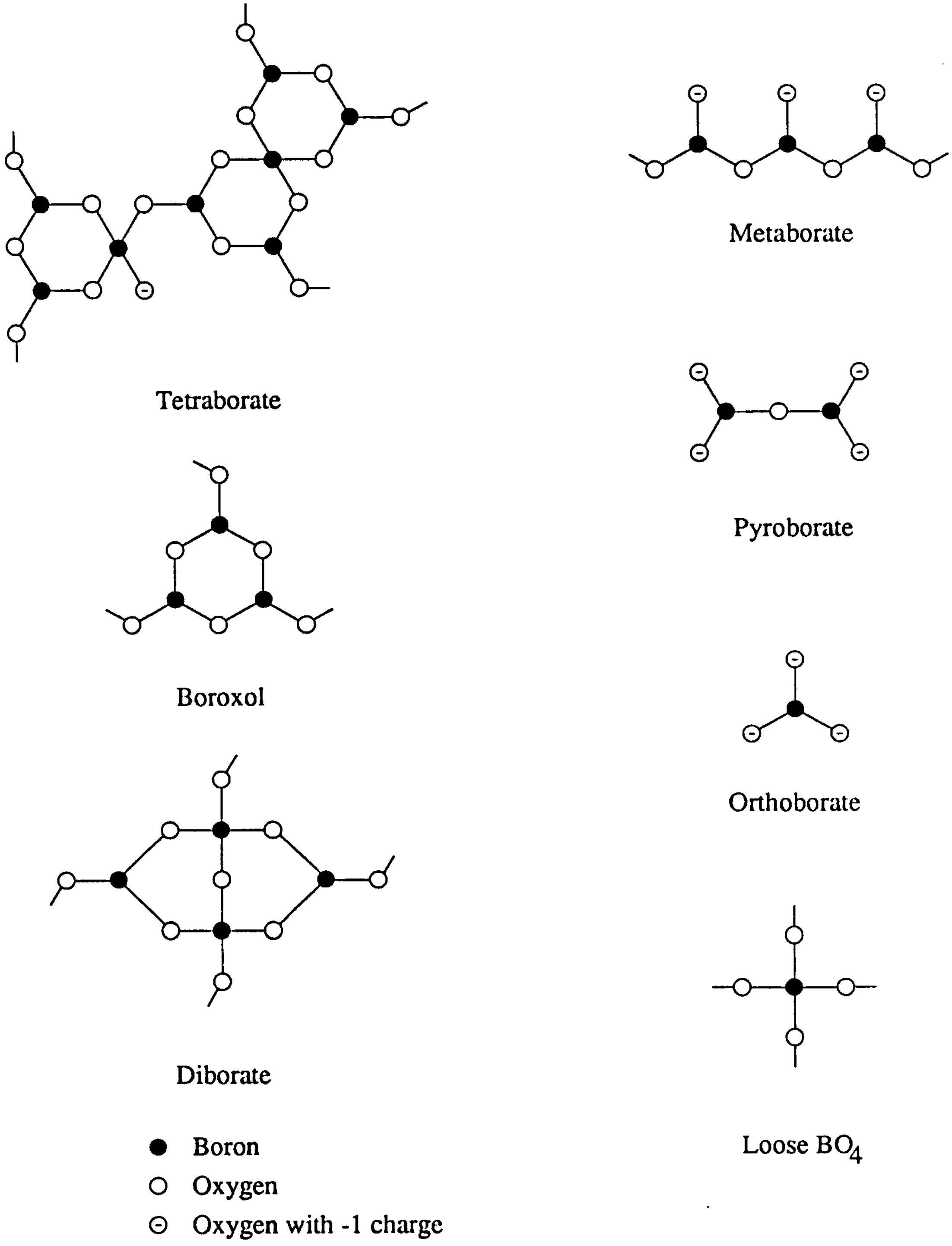

Tetraborate

Metaborate

Pyroborate

Boroxol

Orthoborate

Diborate

Loose BO_4

Figure 8. Two dimensional representations of the basic structures present in alkali borate glasses

alkali borate glasses. This would lead one to believe that systems are similar and that reliable comparisons of some other measured parameters may be made.

The addition of alkali halides to the alkali borate glass appears to have little or no effect on the structure when added in small quantities. The halide ions simply occupy sites between the basic units and the alkali ions are free to move along with those from the alkali oxide added resulting only in an increase in the number of conduction ions present. As with the identity of the alkali metal, the identity of the halide used seems to have little effect on the structure. The exceptions to this are that the heavier the halide, there appears to be a slight lowering of the glass temperature (T_g) and if the amount of alkali halide added becomes much over approximately 25 molar%, crystalline alkali halides can be detected in the glass. The addition of silver halides to silver borate glass has similar effects.

B. Structure of Li_2S+SiS_2 Glass

Much of what is known about the structure of SiS_2 glass has been adapted from the study of silicate glass.[16] The basic structure of the silicate glass in the SiO_4 tetrahedral structure with the silicon atom at the center of four oxygen atoms. If one of these oxygens is connected to another silicon atom, it is referred to as a bridging oxygen atom. This results in the nomenclature for referring to the various silicon sites of $Q^{(n)}$ where n is the number of bridging oxygen atoms attached to the silicon[17] and runs from 0 to 5.

This same nomenclature can be used to describe the silicon sites in the thiosilicate glass where the oxygen atoms are simply replaced with sulfur and $Q^{(2)}$ would refer to a silicon atom in a sulfur tetrahedron with two of the sulfur atoms being bridging sulfur. One major difference between the silicate and the thiosilicate glasses is that $Q^{(1)}$ and $Q^{(3)}$ sites have never been detected in the thiosilicate systems.[18]

Another nomenclature that is used to describe the silicon sites in addition to $Q^{(n)}$ is $E^{(m)}$ where m is the number of edges of the oxygen tetrahedron that are shared with another tetrahedron.[16] Figure 9 shows the various $Q^{(n)}$ $E^{(m)}$ structures.

For pure SiS_2 glass, the ratio of $E^{(0)}$: $E^{(1)}$: $E^{(2)}$ has been measured[19] as 23 : 48 : 29 and is made entirely of $Q^{(4)}$ structures. This ratio for samples similar to the 56% Li_2S+44% SiS_2 sample used here has been measured[16] as 76 : 24 : 0 and the structure becomes entirely $Q^{(2)}$ and $Q^{(0)}$.

Like the borate glasses, the addition of alkali halides does not alter the structure by and measurable amount[18], the alkali ions are allowed to move throughout the glass whereas the halide ions sit in the gaps between the glass structures.

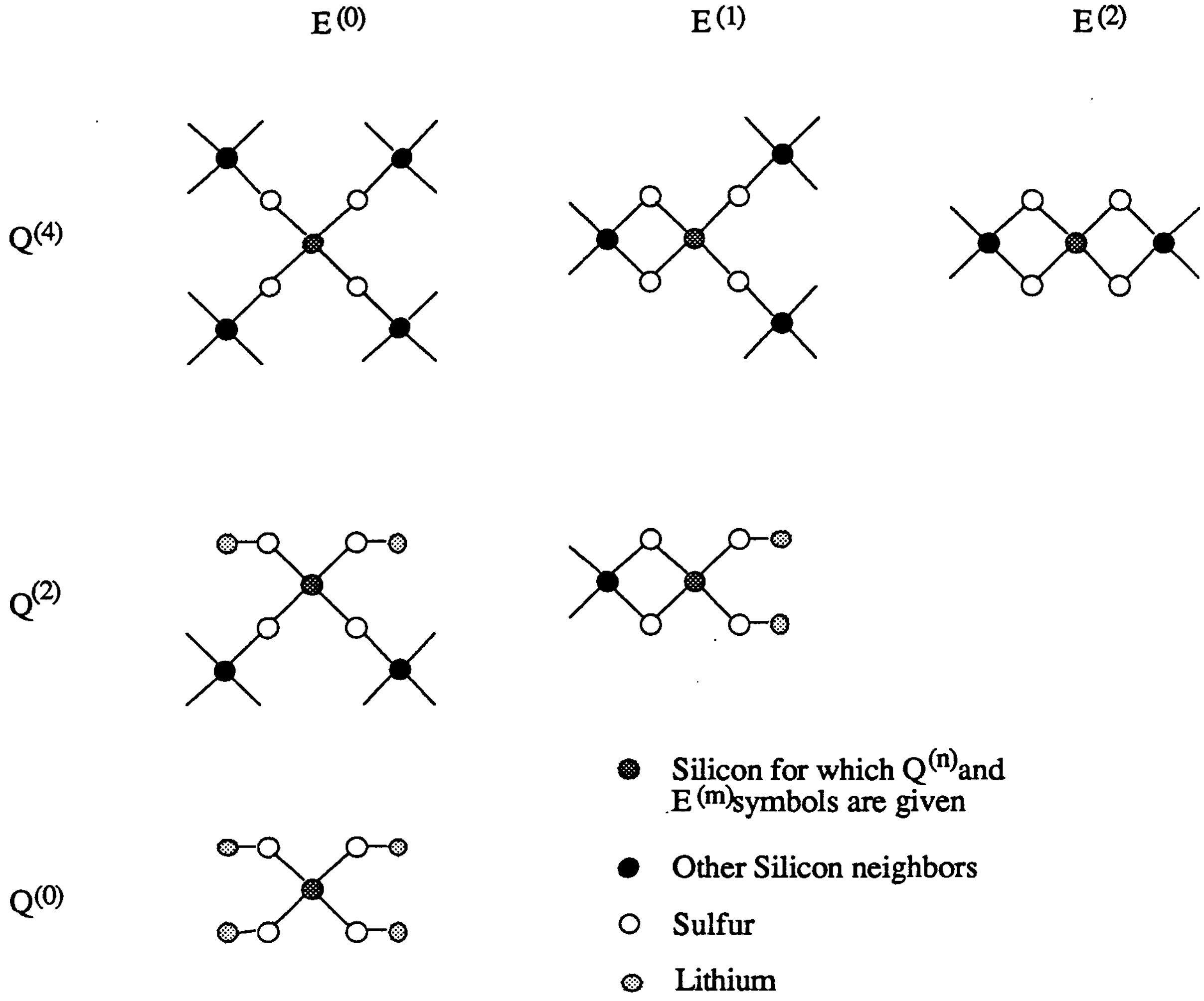

Figure 9. Two dimensional representations of the basic structures present in lithium thiosilicate glasses

Unlike the boron nuclei in borate glasses, the silicon nuclei in the sulfide glasses always lie in sites of high cubic symmetry. Since the most abundant forms silicon have no electric quadrupole moment one must use the different chemical shifts of the spectra for each of the $Q^{(n)}$ sites caused by the interactions of the second nearest neighbors. Using this, the relative abundance of each structure can be determined. It should also be noted that the natural abundance of silicon gives 95% of the nuclei with spin $I = 0$ and only 5% with spin $I = \frac{1}{2}$. Silicon nuclei with spin $I > \frac{1}{2}$ have half-lives of less that 160 minutes.

C. Conductivity of Alkali Borate and Alkali Thiosiliocate Glasses

Measurements of the conductivity of the two glasses will now be examined. The main reason that there is interest in these systems is because they are ionic conductors. Of particular interest to work in NMR is the fact that conductivity measures the same processes but using different parameters thus giving an independent method to compare results with. Results for various d.c. measurements (σ) for the given temperature and the measured activation energy (E_a) are shown in Table 2 for various alkali borate glasses and in Table 3 for various alkali thiosilicate glasses.

Examining these two tables suggests several things. First of all, from Table 2 it is notice that increasing the amount of Li_2O up to ~ 40 molar% increases the conductivity, after which adding more Li_2O lowers the conductivity.[20] One can also notice that by adding a lithium halide to the sample, at least in small quantities, also increases the conductivity[21-23] and that the heavier the halide the greater the increase.[21]

From Table 3 it is noticed that increasing the concentration of Li_2S to as much as 60 molar% also increases the conductivity[25] as does adding lithium halides[27] to the glass.

Data for a.c. conductivity for the 56% Li_2S+44% SiS_2 sample as measured by Hitendra Patel of Iowa State University, Dept. Material Science and Engineering are shown in Figure 10 (the theoretical fit of the data is also shown, this will be discussed in section V.B).

The real conductivity can be written in terms of the electric modulus $M^*(\omega) = \frac{1}{\varepsilon^*(\omega)}$

as

$$\sigma'(\omega) = \omega\varepsilon_0\varepsilon''(\omega) = \omega\varepsilon_0 \frac{M''}{M'^2+M''^2} \qquad (57)$$

Table 2. Tabulation of d.c. conductivity (σ) and activation energy (E_a) measurements for various alkali borate glasses

Glass Composition	$\sigma(\Omega^{-1}\cdot cm^{-1})$	Temperature(K)	E_a(eV)
$B_2O_3+0.67Li_2O$ [40]	5.3×10^{-4}	623	0.86
$B_2O_3+0.74Li_2O$ [40]	2.5×10^{-3}	623	0.77
$B_2O_3+0.82Li_2O$ [40]	1.3×10^{-3}	623	0.87
$B_2O_3+1.00Li_2O$ [40]	5.5×10^{-4}	623	0.88
$B_2O_3+0.70Li_2O+0.70LiCl$ [43]	1×10^{-4}	400	
$B_2O_3+0.70Li_2O+0.70LiCl$ [43]	5×10^{-6}	333	
$B_2O_3+0.50Li_2O$ [44]	2.8×10^{-7}	400	
$B_2O_3+0.57Li_2O+0.85LiCl$ [41]	2×10^{-5}	333	
$B_2O_3+0.85Li_2O+0.28LiCl$ [41]	6×10^{-6}	333	
$B_2O_3+0.57Li_2O+0.57LiCl$ [41]	3×10^{-6}	333	
$B_2O_3+0.42Li_2O+0.28LiCl$ [41]	2×10^{-6}	333	
$B_2O_3+0.57Li_2O+0.21LiCl$ [41]	8×10^{-7}	333	
$B_2O_3+0.56Li_2O+0.08LiF$ [41]	6.3×10^{-4}	573	0.70
$B_2O_3+0.56Li_2O+0.08LiCl$ [41]	1.0×10^{-3}	573	0.60
$B_2O_3+0.56Li_2O+0.08LiBr$ [41]	1.3×10^{-3}	573	0.58
$B_2O_3+0.56Li_2O+0.08LiI$ [41]	3.2×10^{-3}	573	0.52
$B_2O_3+0.74Li_2O$ [42]	7.1×10^{-8}	298	0.60
$B_2O_3+0.74Li_2O$ [42]	6.1×10^{-3}	623	
$B_2O_3+0.57Li_2O+0.22LiCl$ [42]	3×10^{-6}	298	0.50
$B_2O_3+0.57Li_2O+0.22LiCl$ [42]	1.7×10^{-2}	573	
$B_2O_3+0.60Na_2O$ [42]	5.7×10^{-10}	298	0.70
$B_2O_3+0.60Na_2O$ [42]	3.7×10^{-4}	623	
$B_2O_3+0.70Li_2O+0.60LiCl$ [41]			0.48†
$B_2O_3+0.70Li_2O+0.20LiCl$ [41]			0.55†

† Values of E_a are extrapolated from data with slightly lower concentrations of Li_2O.

Table 3. Tabulation of d.c. conductivity (σ) and activation energy (E_a) measurements for various alkali thiosilicate glasses

Glass Composition	$\sigma(\Omega^{-1} \cdot cm^{-1})$	Temperature(K)	E_a(eV)
SiS_2+0.43Li_2S [45]	1.5×10^{-6}	298	0.46
SiS_2+0.67Li_2S [45]	2.8×10^{-5}	298	0.38
SiS_2+1.00Li_2S [45]	1.0×10^{-4}	298	0.32
SiS_2+1.50Li_2S [45]	5.0×10^{-4}	298	0.25
SiS_2+1.00Li_2S [46]	1.5×10^{-4}	298	0.35
SiS_2+1.00Li_2S+0.86LiI[†] [47]	7.1×10^{-4}	298	0.33
SiS_2+1.00Li_2S+0.86LiI[†] [47]	6.3×10^{-4}	298	0.30
SiS_2+1.00Li_2S+0.86LiI[†] [47]	6.9×10^{-4}	298	0.30
SiS_2+1.00Li_2S+0.67LiCl [47]	2.7×10^{-4}	298	0.35
SiS_2+1.50Li_2S+1.07LiI [47]	1.32×10^{-4}	298	0.31
SiS_2+1.50Li_2S [48]	5.3×10^{-4}	298	0.33
SiS_2+0.67Li_2S [49]	6.4×10^{-7}	298	0.47
SiS_2+1.00Li_2S[‡] [49]	6.8×10^{-5}	298	0.34
SiS_2+1.00Li_2S[‡] [49]	1.0×10^{-4}	298	0.32

[†] Measurements done with same composition but different annealing techniques [47].

[‡] Measurements done with same composition but different quenching techniques [49].

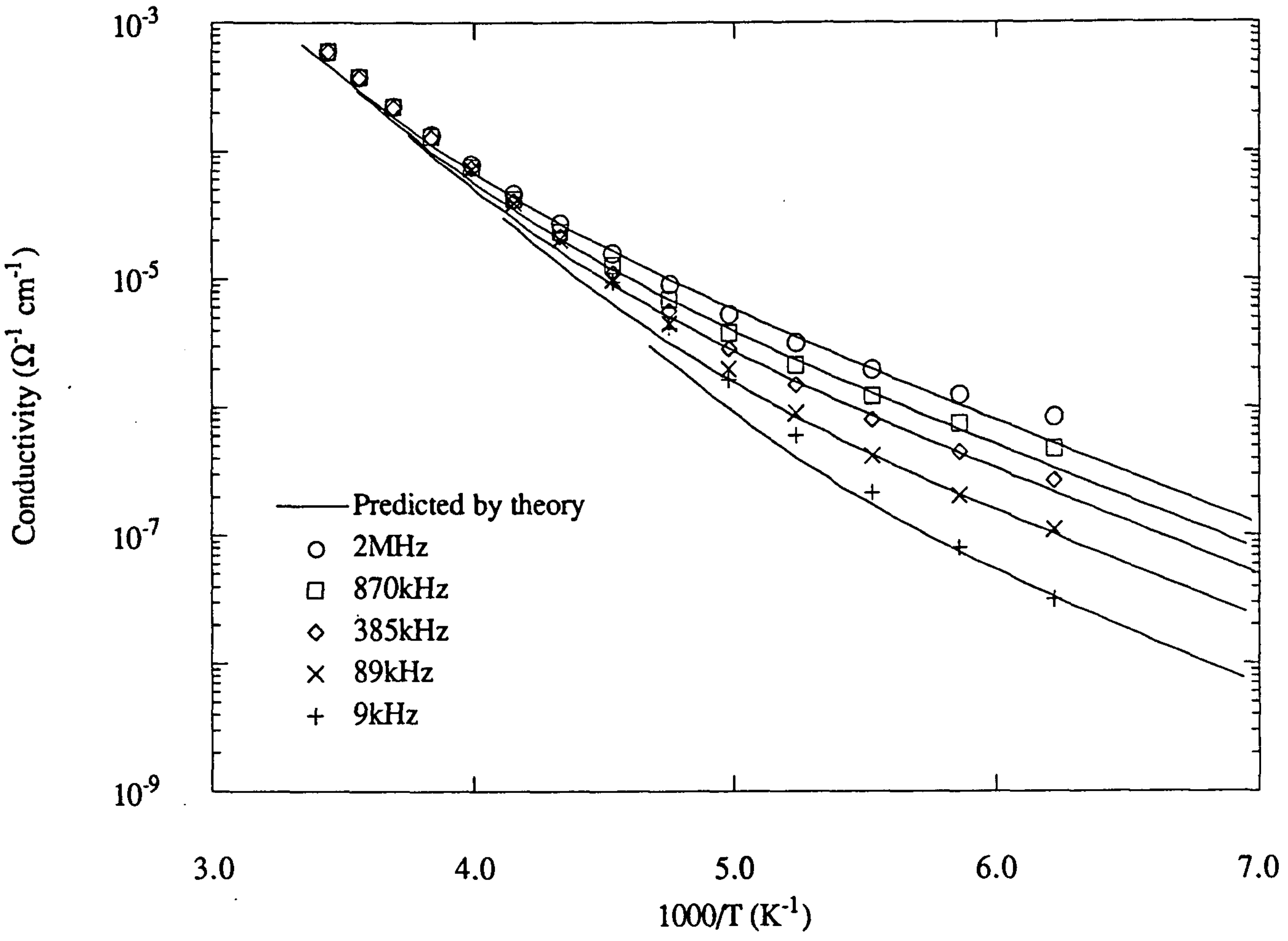

Figure 10. A.C. conductivity vs. 1000/T for 56% Li_2S 44% SiS_2 glass with theoretical fits using the KWW form of the correlation function

where the single prime represents the real component of M, ε or σ and the double prime represents the imaginary component. $M^*(\omega)$ is related to the correlation function G(t) by[30-33]

$$M^*(\omega) = M_\infty \left[1 - \int_0^\infty e^{-i\omega t} \left(- \frac{dG(t)}{dt} \right) dt \right], \tag{58}$$

integrating by parts yields

$$M^*(\omega) = M_\infty \left\{ 1 - \left[e^{-i\omega t}\, G(t) \right]_0^\infty + i\omega \int_0^\infty e^{-i\omega t}\, G(t)\, dt \right\}. \tag{59}$$

If the correlation function has a form like the stretched exponential such that G(0) = 1 and G(t) → 0 as t → ∞, then the term inside the brackets becomes 1 giving

$$M^*(\omega) = M_\infty i\omega \int_0^\infty e^{-i\omega t}\, G(t)\, dt \quad . \tag{60}$$

$M^*(\omega)$ can now be easily divided into it real and imaginary components M' and M" yielding:

$$M'(\omega) = M_\infty \omega \int_0^\infty \sin(\omega t)\, G(t)\, dt \tag{61}$$

$$M''(\omega) = M_\infty \omega \int_0^\infty \cos(\omega t)\, G(t)\, dt \quad . \tag{62}$$

From these equations and Eq.(57) it is found that

$$\sigma'(\omega) = \frac{\varepsilon_0}{M_\infty} \frac{\displaystyle\int_0^\infty \cos(\omega t)\, G(t)\, dt}{\left[\displaystyle\int_0^\infty \sin(\omega t)\, G(t)\, dt \right]^2 + \left[\displaystyle\int_0^\infty \cos(\omega t)\, G(t)\, dt \right]^2} \quad . \tag{63}$$

If the exponential form of G(t) as in Eq.(49) is used, a good fit of the data can not be made but if one assumes the KWW form as in Eq.(52), good agreement between theory and experiment is achieved. The fit of the data is also shown in Figure 10 along with the relevant parameters.

D. Quadrupole Coupling Constant in Borate Glasses

Another quantity of interest in the study of alkali borate glasses is the quadrupole coupling constant. This is a measure of the strength of the EFG at the site of the ^{11}B nuclei and therefore gives information about the neighbors of the nuclei. Measured values of this are shown in Table 4.

Table 4. Quadrupole coupling constant for ^{11}B in BO_3 and BO_4 sites in various borate glasses

Glass Composition	BO_3 sites (MHz)	BO_4 sites (kHz)
B_2O_3+0.05Ag_2O [15]	2.65	
B_2O_3+0.11Ag_2O [15]	2.63	389
B_2O_3+0.17Ag_2O [15]	2.61	389
B_2O_3+0.24Ag_2O [15]	2.60	388
B_2O_3+0.34Ag_2O [15]	2.59	390
B_2O_3+0.36Ag_2O [15]	2.59	390
B_2O_3+0.42Ag_2O [15]	2.59	399
B_2O_3+0.52Ag_2O [15]	2.59	405
B_2O_3+2.50Ag_2O [15]	2.60	390
B_2O_3+5.00Ag_2O [15]	2.57	407
Crystalline B_2O_3[10]	2.71[†]	
Crystalline B_2O_3[10]	2.68[†]	
Crystalline B_2O_3[10]	2.68[†]	

[†] Quadrupole coupling constant was determined at three different resonant frequencies on the same sample.

IV. EXPERIMENTAL PROCEDURES AND RESULTS

The experimental data collected for this paper will now be examined. A description of the preparation of the samples, the equipment used and experimental techniques implemented will be presented first, followed by the data that was taken.

A. Preparation Techniques for Measured Samples

The B_2O_3+0.7Li_2O+0.6LiCl sample was prepared by Masahiro Tatsumisago of the University of Osaka Prefecture, Department of Applied Chemistry starting from 3.481g dried B_2O_3 (Kishada, >90%), 2.586g Li_2CO_3 (Wako, >99%) and 1.272g LiCl (Wako, >99%). The mixture was placed in a platinum crucible and heated at 600°C for 30 minutes, then at 700°C for 30 minutes, 800°C for 30 minutes, 900°C for 30 minutes and finally at 1000°C for 30 minutes. The mixture was then quenched by pouring it onto a metal plate and pressing with another metal plate.

The B_2O_3+0.7Li_2O+0.2LiCl sample was also prepared by Tatsumisago from 3.481g dried B_2O_3, 2.586g Li_2CO_3 and 0.424g LiCl. The mixture was again placed in a platinum crucible and heated for 30 minutes each at 500°C, 700°C, 800°C, 900°C and 980°C and it was then quenched using the same metal plate technique as above.

The 56% Li_2S+44% SiS_2 glass was prepared by H. Patel of Iowa State University, Department of Material Science and Engineering by reacting Si (Alpha, 99.999%) and S (Alpha, 99.999%) in a sealed quartz ampul and then mixed in a mortar with Li_2S (Cerac, 99.9%). The mixture was melted in a vitreous crucible in a Mo wire wound furnace at 1000°C for 5 minutes. It was then quenched into a preheated stainless steel mold.

All samples used for NMR measurements were sealed under vacuum in 10mm quartz ampuls.

B. Instrumentation

The laboratory magnetic field was produced using a Varian Associates V3800 electromagnet with a Varian Associates Fieldial™ Mark II field regulated magnet power supply. The RF field was produced in a custom built probe[54] using a General Radio Company 1061 frequency synthesizer with a frequency range of 0.4MHz to 160MHz. This signal was amplified by a Kalmus Engineering International model 166LP linear pulse RF power amplifier with the pulses controlled by custom built programmable pulser.[55]

The NMR signal was captured by the probe, sent to the receiver[56] and then sent to a Nicholet Instrument Corporation 1170 signal averaging system with a model 171/2 two input signal digitizer. The data was transferred to an DEC Corporation LSI 11/73 computer for its initial analysis.

The temperature within the probe was measured and maintained using an Omega Engineering series CN-2010 programmable temperature controller[54] and it was independently measured using a separate thermocouple connected to a Keithly Instruments 195A digital multimeter and an Omega Engineering Omega-CJ cold junction compensator.

C. Experimental Methods and Data Analysis

Data was taken with the above equipment using several different techniques. Some spectra were taken with the ALVIN[57] software using an off resonance fourier transform technique. The RF pulses were set at a frequency slightly off the Larmor frequency for the magnetic field which caused a ringing in the free induction decay (FID) that was captured by the digitizer and stored. This was then put through a fast fourier transform (FFT) routine with the output being the frequency spectrum of the nucleus in the material.

Other spectra were obtained using a spin echo technique where a 90° pulse is given and at some later time less than T_2 another 90° pulse is given to cause an echo. This echo recreates the shape of the initial FID but because the echo occurs long after the pulse, it is not affected by the dead time of the receiver and thus earlier times can be detected and a wider frequency range detected.

Spin lattice relaxation data was taken using two similar methods; inversion-recovery and picket fence. Inversion-recovery consists of using a 180° pulse to invert the magnetization into the -Z direction. After waiting some time t, a 90° pulse was used to rotate the magnetization into the X-Y plane. Immediately after that, the magnitude of the signal was measured and the sample is allowed to recover back to its equilibrium magnetization M_0. This was repeated at even increments of time t allowing a measurement of magnetization in the Z direction as a function of time. Under ideal conditions, one would get a plot similar to that in Figure 11a with T_1 shown as defined previously.

With the picket fence method, a train of 90° pulses alternating between the x' and y' directions separated by a short time of approximately T_2 was used. This resulted in the individual magnetic moments becoming dephased and the resulting magnetization being zero. Following the pulse train by a time t, another 90° pulse was used to rotate the magnetization into the X-Y plane where it could be measured. This was repeated for even

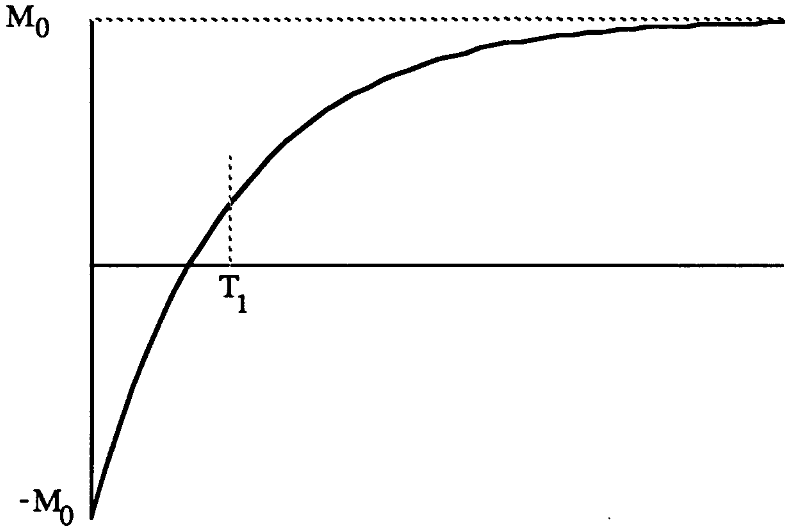

Figure 11a. Magnetization vs. time for inversion-recovery

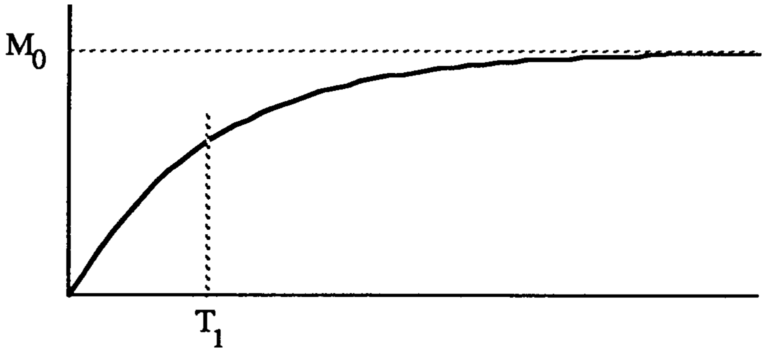

Figure 11b. Magnetization vs. time for picket fence

increments of time t again allowing a measurement of magnetization in the Z direction as a function of time. An ideal plot of the magnetization for the picket fence is shown in Figure 11b.

Whether using the inversion-recovery or the picket fence method, the magnetization versus time data were analyzed with the BIONIC[58] software with a curve fitting routine that fit the data to an exponential function and gave a best fit value for T_1.

Each of the two methods has its relative advantages and disadvantages. An advantage of the inversion-recovery method is that the magnetization goes from $-M_0$ to $+M_0$ and therefore gives a greater range of values from which to evaluate T_1. The picket fence method only gives values of the magnetization from 0 to M_0. A disadvantage of inversion-recovery is that the sample must be allowed to recover back to equilibrium before another data point can be taken. Usually this requires letting the sample sit for a time between five and ten times that of T_1. If T_1 is long, this can slow down the data taking process. Since the magnetization in the picket fence method is essentially scrambled until it is zero, there is no need to have the sample at equilibrium when the pulses start for the next data point, therefore data can be taken much more quickly. The picket fence method is also useful when wide spectral lines are present and one 180° pulse will not completely invert the magnetization.

D. Experimental Results for $B_2O_3+0.7Li_2O+XLiCl$

1. NMR spectra

The experimental data are now examined. The NMR spectra for ^{11}B in $B_2O_3+0.7Li_2O+XLiCl$ were taken using the off resonance method described above for both the $X = 0.2$ and $X = 0.6$ samples at 24.0MHz and for the $X = 0.6$ sample only at 32.5MHz and 12.2MHz. The 32.5MHz spectra were taken with an oscillator frequency of 32.540MHz, the 24.0MHz spectra with an oscillator frequency of 24.050MHz and the 12.2MHz spectra with an oscillator frequency of 12.250MHz. In all cases, 2048 data points were taken in the time domain with $\Delta t = 1\mu s$ per channel which results in a Nyquist frequency of 500kHz. An 8K FFT was used to transform the data to the frequency domain resulting in a frequency width per channel of 122.07Hz.

The spectra were taken at several different temperatures ranging from 100K to 500K but showed no noticeable temperature dependence and for this reason the individual spectra for each frequency were averaged together to get the spectra shown in Figures 12-14. The

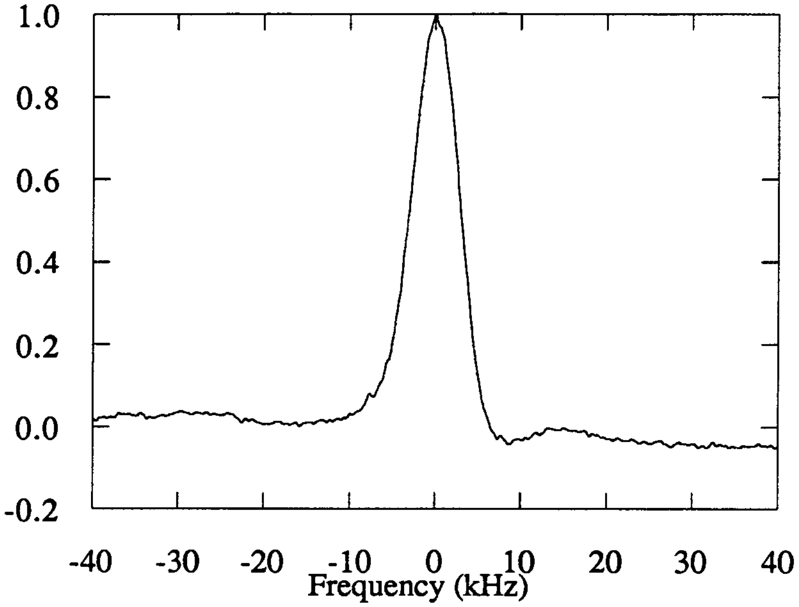

Figure 12. ^{11}B spectrum for B_2O_3+0.7Li_2O+0.6LiCl glass at 24.0MHz

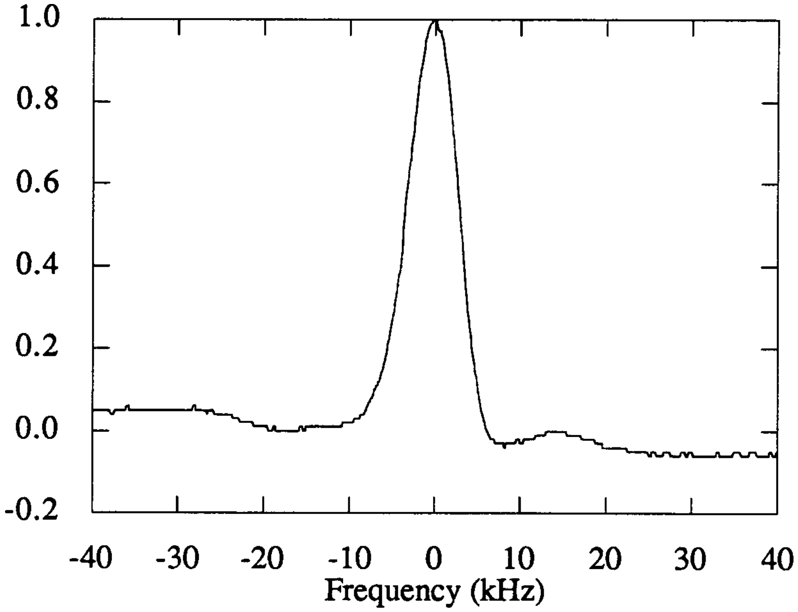

Figure 13. ^{11}B spectrum for B_2O_3+0.7Li_2O+0.2LiCl glass at 24.0MHz

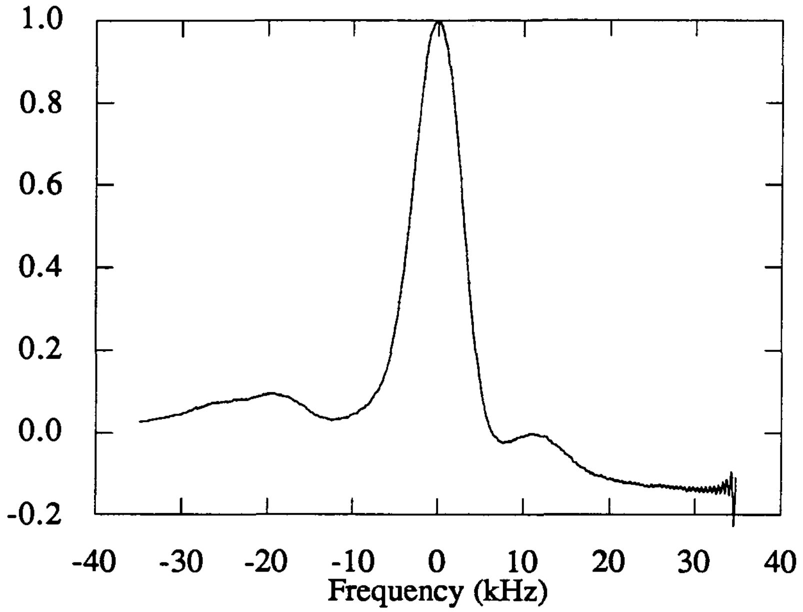

Figure 14. ^{11}B spectrum for $B_2O_3+0.7Li_2O+0.6LiCl$ glass at 32.5MHz

Table 5. Summary of measurements of NMR spectra

$B_2O_3+0.7Li_2O+XLiCl$	Frequency	Width of Central Peak	Separation of Side Peaks
X = 0.6	32.5MHz	6.89kHz	30kHz
X = 0.6	24.0MHz	6.53kHz	45kHz
X = 0.2	24.0MHz	6.53kHz	48kHz
X = 0.6	12.2MHz	~6kHz	no peaks seen

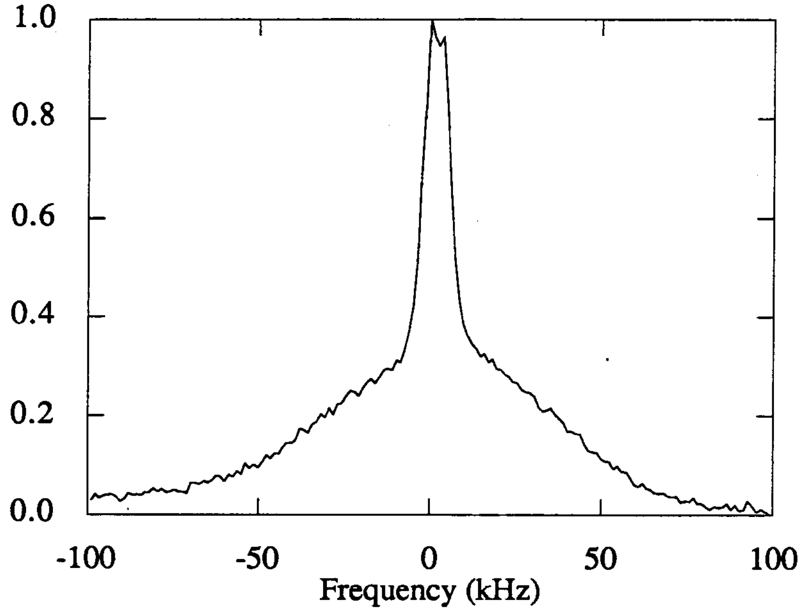

Figure 15. ^{7}Li spectrum for B_2O_3+0.7Li_2O+0.6LiCl glass at 22.0MHz and ~80K

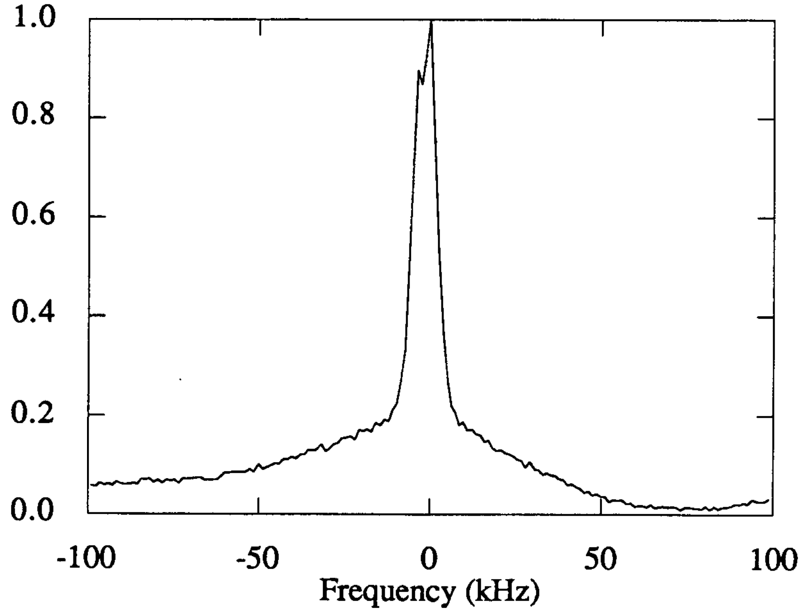

Figure 16. ^{7}Li spectrum for B_2O_3+0.7Li_2O+0.2LiCl glass at 22.0MHz and ~80K

spectra for 12.2MHz had no structures other than the central peak and are not shown. Each of the spectra represents only 655 of the data points since the remaining truncated data points showed no structure.

In each spectrum there are two measurements of interest, the width of the central peak and the separation of the two side peaks. The results of these measurements are shown in Table 5. The interpretation of the spectra will be done in the next section.

NMR spectra for ^{7}Li were taken at 22.0MHz using the spin echo technique where the two pulses were separated by 30μs and a 33μs delay was used before capturing the signal. ALVIN[57] was used to perform the complex FFT giving the spectra for the $X = 0.6$ sample in Figure 15 and for the $X = 0.2$ sample in Figure 16.

2. Spin lattice relaxation measurements

Measurements of the spin lattice relaxation time T_1 were taken for both ^{11}B and for ^{7}Li in B_2O_3+0.7Li_2O+XLiCl. In the $X = 0.6$ sample, the ^{11}B data were taken at 12.2MHz, 24.0MHz and 32.5MHz and in the $X = 0.2$ sample at 32.5MHz using the picket fence method described above. The picket fence consisted of a series of 46 pulses alternating between the x' and y' directions followed after the delay by a single pulse in the x' direction. The individual pulses were each 2.5μs in length separated by a 100μs delay. The results of the ^{11}B relaxation time presented represent only the boron nuclei in the BO_4 structures. The pulse train saturated the central transition and part of the satellites giving a recovery of the nuclear magnetization that was slightly nonexponential. T_1 was determined by forcing the recovery to fit the exponential function which leads to a systematic error that is larger than that for the other T_1 measurements reported here. In this case, $\frac{1}{T_1} \approx \frac{2}{5}(W_1 + 4W_2)$ which follows from Eq.(40). Figure 17 shows the T_1 results for the $X = 0.6$ sample at the three measured frequencies and Figure 18 shows the T_1 results of both the $X = 0.6$ and the $X = 0.2$ samples at 32.5MHz. Note that the 32.5MHz data for the X=0.6 sample shown in the two figures are identical.

The ^{7}Li T_1 data were taken using the inversion-recovery method at 4.0MHz, 12.2MHz and 40.0MHz for the $X = 0.6$ sample and at 12.2MHz for the $X = 0.2$ sample. Again the recovery of the nuclear magnetization fit the exponential function very well. At high temperatures both the central and the satellite lines are irradiated and $\frac{1}{T_1} = 2W_M$ which follows from Eq.(37). At low temperatures first order quadrupole

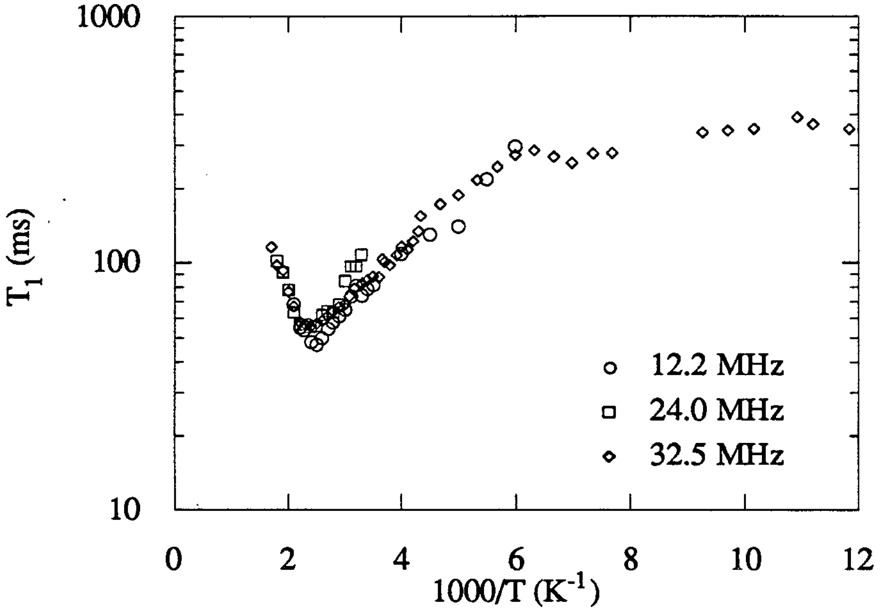

Figure 17. ^{11}B T_1 data for B_2O_3+0.7Li_2O+0.6LiCl glass

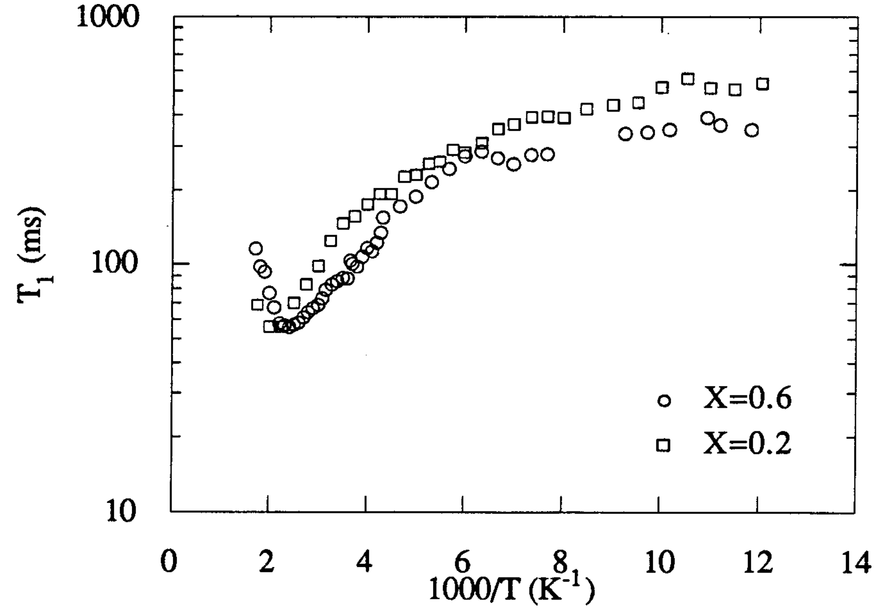

Figure 18. ^{11}B T_1 data for B_2O_3+0.7Li_2O+XLiCl glass at 32.5MHz

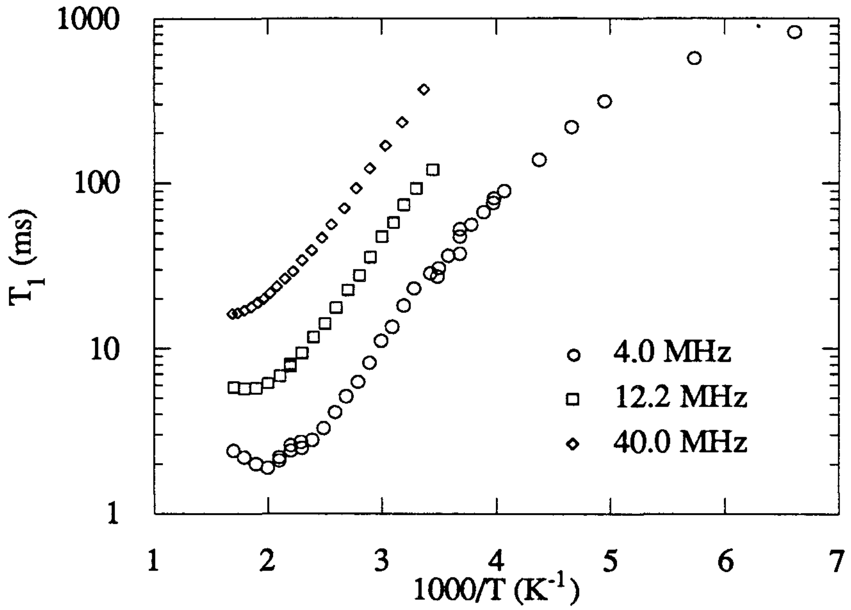

Figure 19. ^{7}Li T_1 data for B_2O_3+0.7Li_2O+0.6LiCl glass

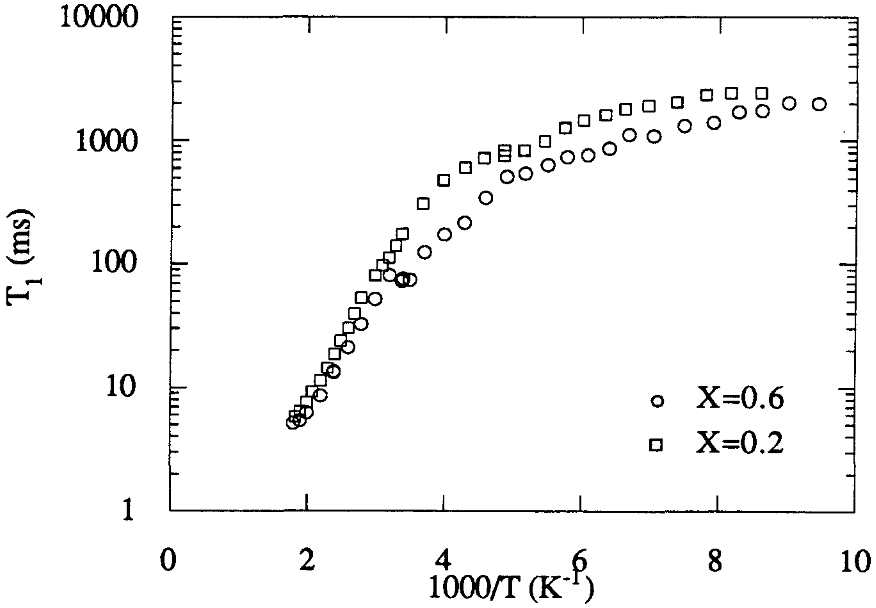

Figure 20. ^{7}Li T_1 data for B_2O_3+0.7Li_2O+XLiCl glass at 12.2 MHz

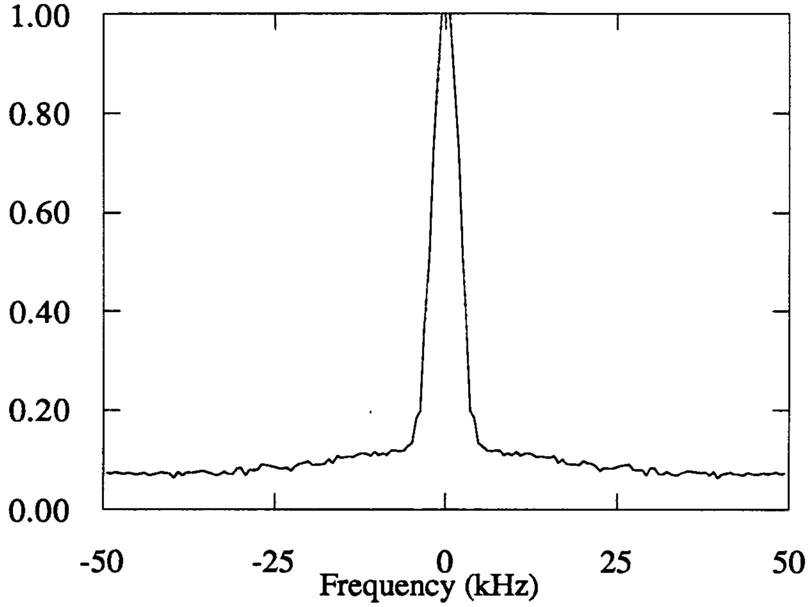

Figure 21. ^{7}Li spectrum for 56% Li_2S 44% SiS_2 glass at 22.0MHz and ~80K

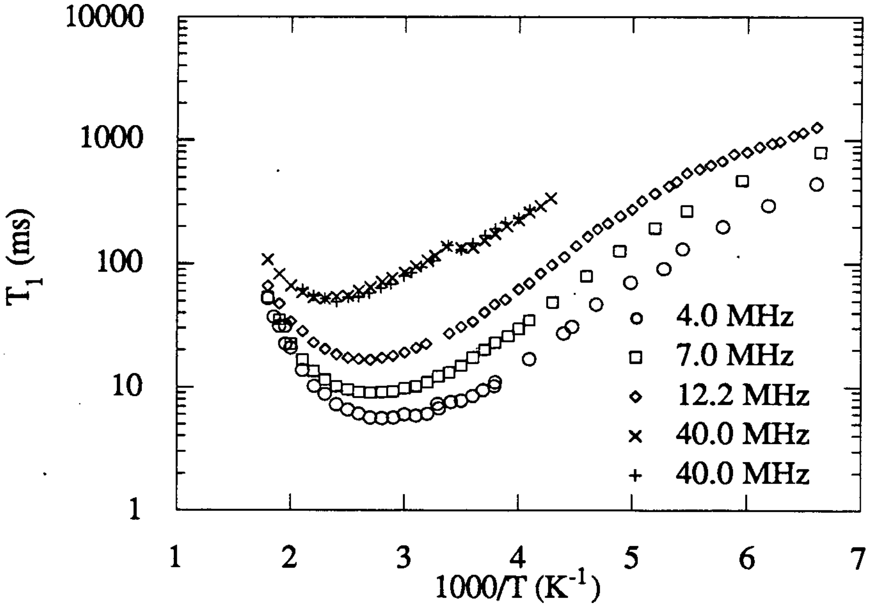

Figure 22. ^{7}Li T_1 data for 56% Li_2S 44% SiS_2 glass

effects are present as shown in Figures 15 and 16. The distribution of the satellite transitions is over a range of about 75kHz which is small enough so that the satellites and the central line can be saturated using a short sequence of 90° pulses. The T_1 results for the $X = 0.6$ sample at the three measured frequencies are shown in Figure 19 and the results of both the $X = 0.6$ and $X = 0.2$ samples at 12.2MHz are shown in Figure 20. Note that the 12.2MHz data for the $X = 0.6$ sample shown in the two figures is not the same. This is due to the fact that since the data shown in Figure 19 were taken using an older sample and the data shown in Figure 20 using a newer sample, the 12.2MHz data were repeated to see if there were any noticeable differences; none were observed. All ^{11}B data were taken using the newer sample.

E. Experimental Results for 56% Li_2S+44% SiS_2

1. NMR spectra

As with the ^7Li spectra for the lithium chloroborate glass, the ^7Li spectra for the lithium thiosilicate glass was also taken using the spin echo technique. The separation of the two 90° pulses was 30μs and the delay before digitizing the echo was 31μs. At temperatures above ~ 200K only the central line was seen and its broadening was due mainly to the inhomogeneity of the external magnetic field but at low temperatures first order quadrupole effects could be seen. A spectrum taken at ~ 80K is shown in Figure 21.

2. Spin lattice relaxation measurements

Measurements of T_1 for ^7Li in 56% Li_2S+44% SiS_2 were taken at 4.0MHz, 7.0MHz, 12.2MHz and 40.0MHz using the inversion recovery method. As with ^7Li in the previous samples the recovery of the nuclear magnetization for each data point fit the exponential function very well. Again, at low temperatures first order quadrupole effects are present (Figure 21.) but the broadening is ~ 35kHz which is small enough so that the satellite and central line can be saturated using a short pulse sequence. The results of these measurements are shown in Figure 22.

V. DISCUSSION OF EXPERIMENTAL RESULTS

In this section the data presented in the previous section shall be interpreted. All of the ^{7}Li T_1 measurements can be analyzed using the stretched exponential form of the correlation function and as shall be seen, these results agree well with the d.c. and a.c. conductivity measurements done on similar samples. The ^{11}B T_1 data indicates that the boron nuclei are not relaxed by the lithium long range diffusional motion. A good fit of the results is obtained by applying a Raman two phonon relaxation mechanism in the presence of strong damping.

A. B_2O_3+Li_2O+XLiCl Glasses

1. NMR spectra

The ^{11}B spectra in the lithium chloroborate glasses have three structures of interest, the central peak and the two side peaks. These can be interpreted if it is assumed that there are ^{11}B nuclei in two different environments. The large central peak is the powder pattern from nuclei that are sitting in sites that have very small EFGs and therefore there is no quadrupole splitting of the central transition as in Figure 5b. These nuclei are sitting in the center of four oxygen atoms in the BO_4 sites discussed in Section III.A. Because these oxygen atoms form a tetrahedron with an ^{11}B nucleus at its center, the EFG due to the oxygen at the ^{11}B site is zero. Any EFG that is present must therefore be due to some other atom which is farther away that the oxygen and since the EFG drops off as $\frac{1}{r^3}$, the EFG due to these other atoms must be very small.

The two side peaks are therefore the powder pattern due to ^{11}B nuclei in the less symmetric BO_3 sites. The EFG at the ^{11}B site due to the three oxygen atoms is not zero and therefore the central peak is split into the two side peaks. As stated in Eq.(28), the separation of these two peaks should be

$$\Delta\nu = \frac{25\nu_Q^2}{48\nu_0} \tag{64}$$

which results in $\nu_Q = 1.4$MHz from the 32.5MHz spectrum and $\nu_Q = 1.5$MHz from the 24.0MHz spectra. Since the 32.5MHz spectra have larger more easily measured side peaks and also since the average was taken from more individual spectra, the result of 1.4MHz should be weighted more than 1.5MHz giving a weighted average of ν_Q = 1.4MHz.

It is now asked why the quadrupole splitting was not seen in the 12.2MHz spectra. Assuming that ν_Q = 1.4MHz, the side peaks should have appeared at ν^I = 12.23MHz and at ν^{II} = 12.19MHz which are well within the frequency window of the FFT. As the resonance frequency gets lower, the separation of the side peaks will get larger resulting in the signal from the same number of nuclei being spread out over a larger frequency range as shown in Figure 6b giving a lower peak height. Even in the 24.0MHz spectra the quadrupole split peaks are difficult to see.

Another point which must be explained is the lack of first order quadrupole satellite peaks. If ν_Q = 1.4MHz the satellite peaks due to the nuclei in the BO_3 sites should appear at $\nu_0 \pm 0.7$MHz. This is well outside the 0.250MHz range that the FFT gave for all spectra. Even if the FFT range were larger, the peaks would be difficult to detect due to of the narrow frequency width of both the RF pulse and the receiver.

Values of ν_Q for ^{11}B nuclei in BO_4 sites have been reported by Kim and Bray[15] where they found ν_Q = 200kHz which should give the satellite peaks at $\nu_0 \pm 0.1$MHz. The ν_0 - 0.1MHz peak is within the limits of the FFT for all spectra taken but is not seen in these experiments due to the large frequency range over which they are spread as seen in Figure 5a. The intensity of these peaks is spread over a range of $\frac{3}{2}\nu_Q$ and according to Abragam[47] the intensity of a satellite peak is only $\frac{3}{4}$ that of the central peak for an $I = \frac{3}{2}$ nucleus resulting in satellite peaks of very low height which and probably not detectable using this method of NMR spectroscopy.

2. ^{7}Li spin lattice relaxation

Data for the spin lattice relaxation time of ^7Li in B_2O_3+0.7Li_2O+0.6LiCl can not be adequately explained by using a correlation function that is an exponential as in the BPP theory (section II.C.3) but it can be explained quite well if one assumes the KWW form of the correlation function (section II.C.4).

To fit the data, the following relations which can be derived from Eq.(48) and Eq.(54) are used:

$$\omega_L \tau_c \ll 1 \qquad T_1 \propto \tau_c^{-1} \tag{65}$$

$$T_{1max} \approx 0.64 \qquad T_1 \propto e\left(\frac{E_a}{k_B T_{min}}\right) \tag{66}$$

$$\omega_L \tau_c \gg 1 \qquad T_1 \propto \omega_L^{(1+\beta)} \tau_c^{\beta} \tag{67}$$

where T_{1min} is the minimum value of T_1 occurring at temperature T_{min}. Eq.(65) describes the behavior on the high temperature side of the minimum and Eq.(67) describes the behavior on the low temperature side. From this it can be seen that the slope on the high temperature side is proportional to E_a whereas the slope on the low temperature side goes as βE_a. Another method for determining β is from the frequency dependence of T_1 at constant temperature and therefore constant τ_c on the low temperature side of the minimum (see Eq.(67)).

Since the glass temperature of B_2O_3+0.7Li_2O+XLiCl is only about 650K and T_{1min} occurs at temperatures above 500K, data on the high temperature side of T_{1min} can only be taken over a limited range and therefore the slope can not be determined. By looking at the frequency dependence of T_1 at temperatures below T_{1min} a value of $\beta = 0.36$ has been determined (see Figure 23). Of the three temperatures shown in Figure 23, the 555K data was not used since it is too close to the minimum and the and in the other two temperatures, the 40.0MHz data points are not weighed as heavily as the 12.2MHz and the 4.0MHz points due to additional effects on T_1 that occur at high frequencies.[59] Once β has been determined the other parameters can be found from the data; these parameters are summarized in Table 6 and a graph showing both the data and the theoretical fits are shown in Figure 24.

Fitting the ^{7}Li T_1 data for B_2O_3+0.7Li_2O+0.2LiCl could not be done as accurately as in the X = 0.6 sample due to there being only one frequency at which data was taken and the high temperature limit imposed by the glass temperature. If it is assumed that the same values for β and E_a will be obtained for the X = 0.2 sample as were obtained for the X = 0.6 sample, the remaining parameters can be determined. These are also summarized in Table 6 and the data for both the X = 0.2 and X = 0.6 samples taken at 32.5MHz are shown with their theoretical fits are shown in Figure 25.

The value of A obtained from fitting the data allows one to determine the dominant interaction that is responsible for the lithium relaxation. For dipole dipole interactions, A is related to the rigid lattice second moment (see section II.B.2) giving $A = \langle \omega_d^2 \rangle$ but for

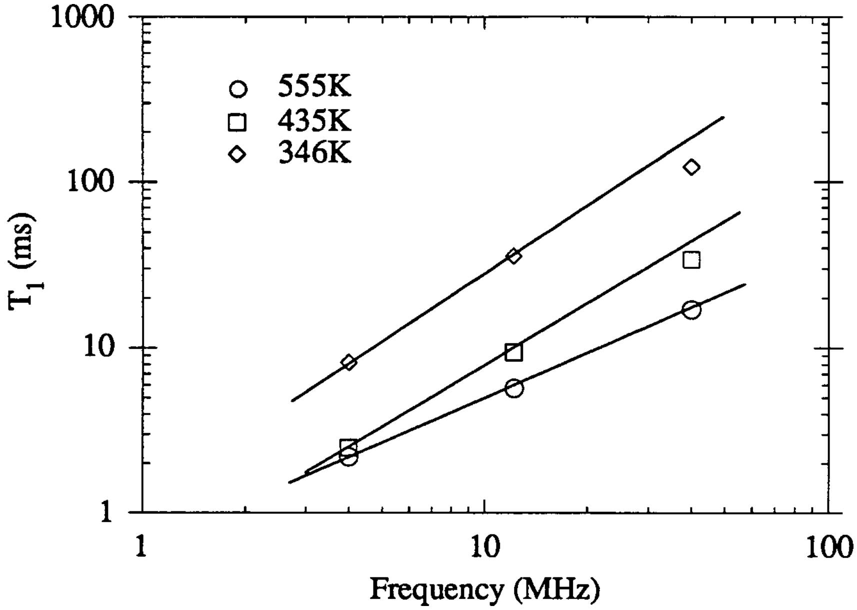

Figure 23. T_1 vs. frequency for ^{7}Li in B_2O_3+0.7Li_2O+0.6LiCl

Table 6. Summary of parameters used to fit ^{7}Li T_1 data in B_2O_3+0.7Li_2O+XLiCl

Glass Composition	β	E_a(eV)	τ_0(sec)	$A(\frac{rad}{sec})^2$
B_2O_3+0.7Li_2O+0.6LiCl	0.36	0.64	8×10^{-15}	11.5×10^{9}
B_2O_3+0.7Li_2O+0.2LiCl	0.36	0.64	24×10^{-15}	11.5×10^{9}

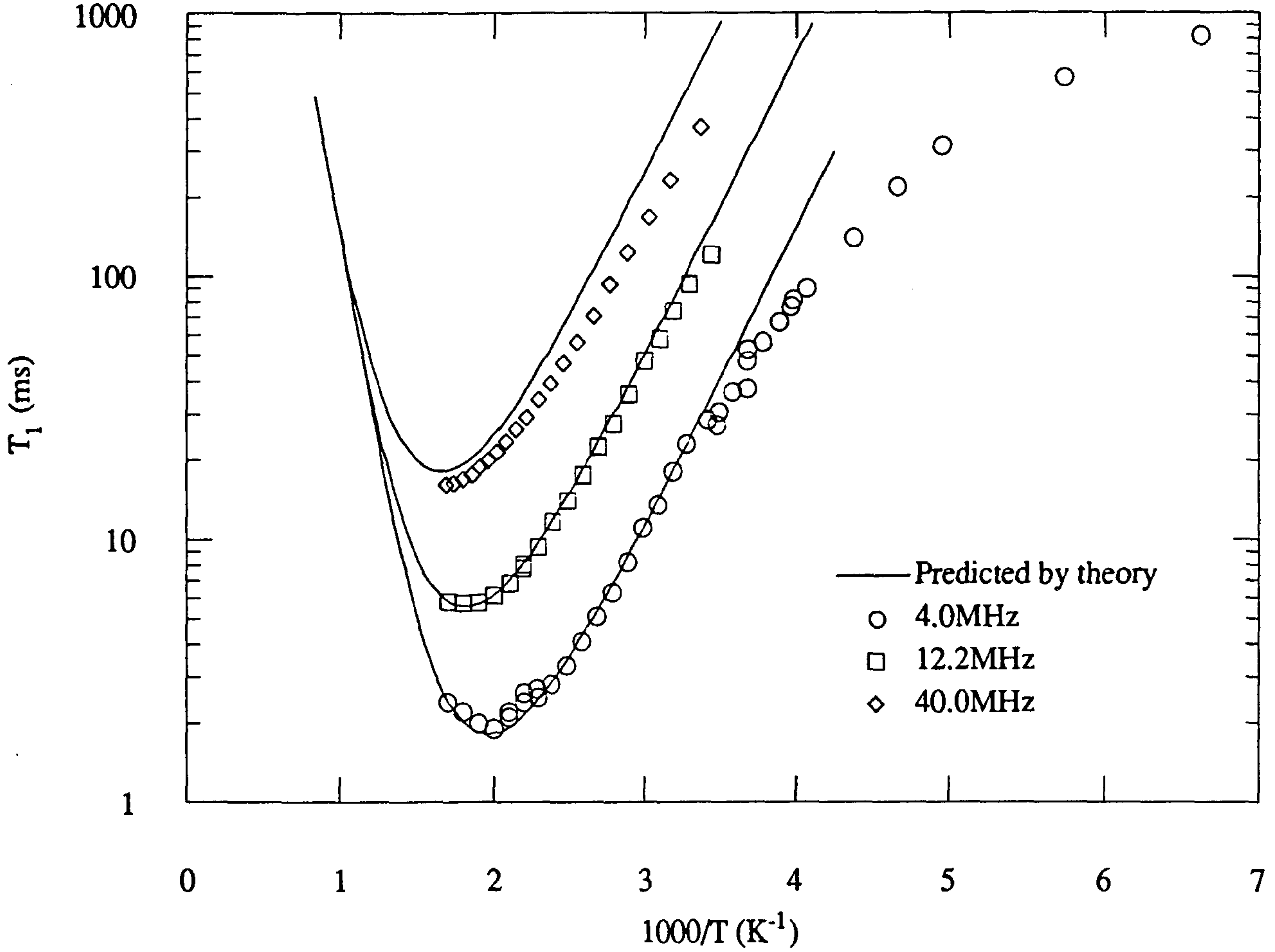

Figure 24. ^{7}Li T_1 data for B_2O_3+0.7Li_2O+0.6LiCl glass with theoretical fits using the KWW form of the correlation function.

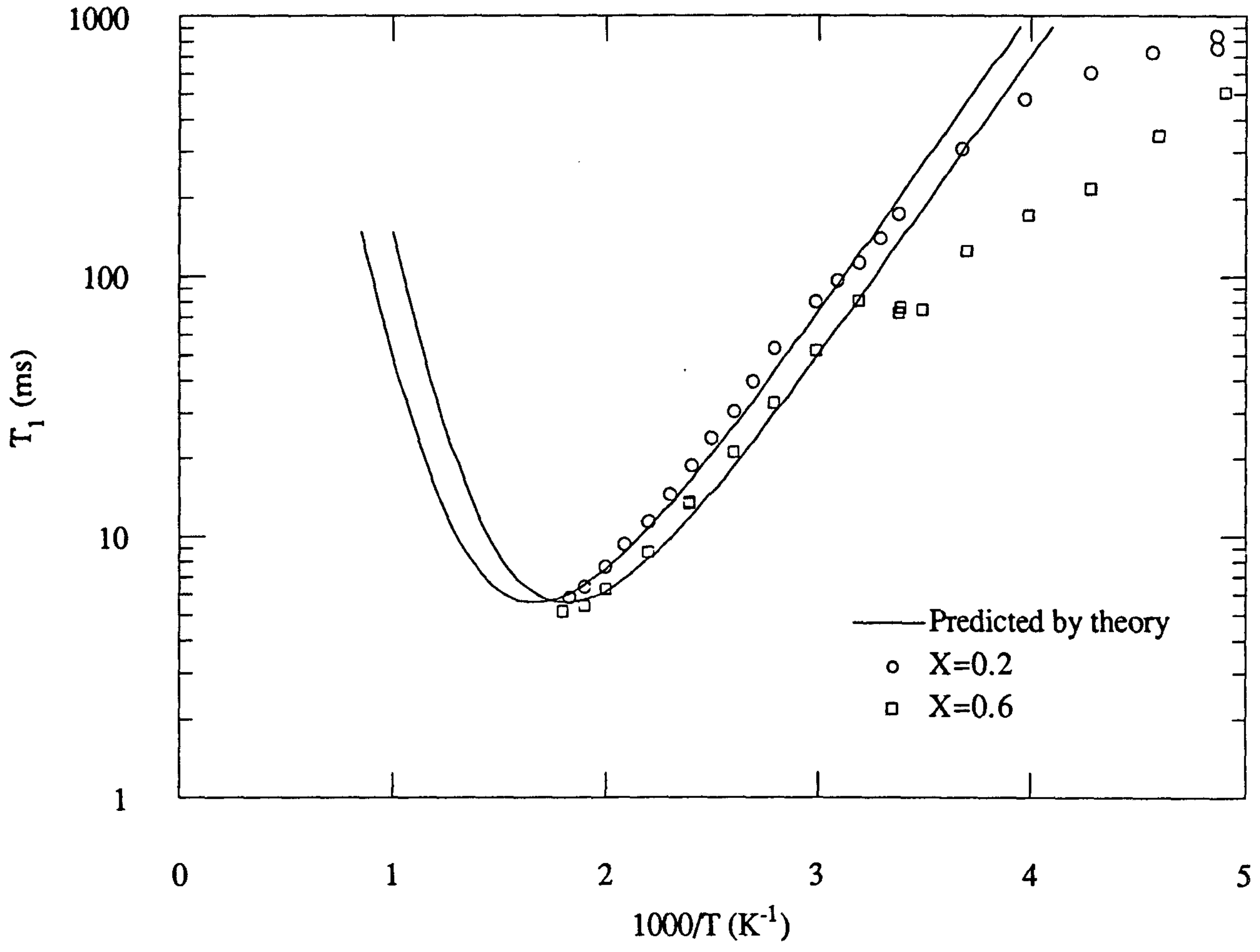

Figure 25. ^{7}Li T_1 data for B_2O_3+0.7Li_2O+XLiCl glass for X=0.2 and X=0.6 at 12.2MHz with theoretical fits using the KWW form of the correlation function

quadrupole interactions $A \approx \langle \omega_Q{}^2 \rangle$ where ω_Q is the root mean square of the time dependent quadrupole interaction energy. The value of A obtained is much too large for dipole-dipole interactions but is of the correct order of magnitude for the quadrupole interactions responsible for the ^{7}Li spectra shown in Figures 15 and 16 therefore it is concluded that the dominant interaction driving the spin lattice relaxation of ^{7}Li is the interactions of its electric quadrupole moment with the fluctuating EFGs due to the lithium diffusive motion through the glass.

3. ^{11}B spin lattice relaxation

The ^{11}B nuclear spin lattice relaxation time as a function of temperature as shown in Figures 17 and 18 show almost no dependence on the frequency of the measurements indicating that the mechanism responsible for the relaxation must be different than that which is responsible for the relaxation of the ^{7}Li. This seems like a reasonable assumption since the lithium relaxation is due to its diffusional motion and the boron nuclei are fixed within the BO_3 and BO_4 sites.

It has been argued[38,39] that the relaxation of the boron nuclei is due to a Raman process involving the excitation and de-excitation of two internal vibrational or librational modes. A successful model for the relaxation of ^{11}B was predicted by Rubinstein et al.[38,39] which involved heavily damped low frequency phonons. By using the Van Kranendonk theory[60] for insulators, the following relation was found:

$$\frac{1}{T_1} = \frac{B}{\pi} T^2 \left\{ 2\tan^{-1}\left(\frac{\varepsilon}{\hbar\Delta}\right) - \frac{\hbar\Delta}{\varepsilon} \ln\left[1 + \frac{\varepsilon^2}{\hbar^2\Delta^2}\right]\right\} \tag{68}$$

where Δ is the phonon damping frequency and could be affected by the long range lithium diffusion. It is assumed that Δ is thermally activated giving

$$\Delta \equiv \Delta_0 e^{-\frac{\bar{E}}{k_B T}} \tag{69}$$

where $\bar{E}$ is the average activation energy. ε is the width of the dispersion for the optical modes and B is the interaction strength between the ^{11}B electric quadrupole moment and the local EFG. The parameters from a best fit of the experimental data for the $X = 0.6$ sample are summarized in Table 7 and the theoretical curve is shown with the data in Figure

Table 7. Summary of parameters used to fit ^{11}B T_1 data in B_2O_3+0.7Li_2O+XLiCl

Glass Composition	B(sec^{-1} K^{-2})	$\frac{\hbar\Delta_0}{\varepsilon}$	$\bar{E}$(eV)
B_2O_3+0.7Li_2O+0.6LiCl	2.8×10^{-4}	800	0.31
B_2O_3+0.7Li_2O+0.2LiCl	1.9×10^{-4}	200	0.31

Table 8 Summary of parameters used to fit ^7Li T_1 data and a.c. conductivity data in 56% Li_2S+44% SiS_2

Data Type	β	E_a(eV)	τ_0(sec)	A$(\frac{rad}{sec})^2$ or B(sec Ω^{-1} cm^{-1})
Relaxation Time	0.36	0.39	4.5×10^{-14}	3.8×10^9
Conductivity	0.46	0.35	2.0×10^{-15}	2.5×10^{-12}

26. The data for the X = 0.2 sample can also be fit with this theory by keeping $\bar{E}$ the same but allowing the other parameters to vary. These results are also summarized in Table 7 and the theoretical curve with data shown in Figure 27.

B. 56% Li_2S+44% SiS_2 Glass

As with the relaxation of ^7Li in the chloroborate glasses, the spin lattice relaxation data for ^7Li in the 56% Li_2S+44% SiS_2 glass can not be described by a simple exponential function but a good fit of the data can be obtained by using the KWW form of the correlation function. This is also true of the conductivity data shown in Figure 10 however, the values of β and τ_c used for the NMR data are not the same as those used for the conductivity data.

To fit the T_1 data, Eq.(65), Eq.(66) and Eq.(67) were used. For the conductivity data, the following relations were derived from Eq.(54) and Eq.(67):

$$\omega \rightarrow 0 \qquad \sigma(\omega) \equiv \sigma_{d.c.} \propto \tau_c^{-1} \qquad (70)$$

$$\omega\tau_c \gg 1 \qquad \sigma(\omega) \propto \omega^{(1-\beta)}\tau_c^{-\beta}. \qquad (71)$$

The values of E_a and β can be more easily obtained from the T_1 measurements for the lithium thiosilicate glass than for the lithium chloroborate since there exists data on both the high and low temperature sides of T_{1min}. E_a can be determined from the slope on the high temperature side and β from the ratio of the high and low temperature sides. The parameters used in the fits are summarized in Table 8 and the T_1 data along with the theoretical curves are shown in Figure 28; the conductivity data with theoretical curves was presented in Figure 10.

The bump that appears in the 40.0MHz data is a real effect and seems to be due to some extra contribution to T_1 that is seen only at higher frequencies[59] and could be studied in more detail at some later time.

The relations given in Eq.(65) and Eq.(67) and in Eq.(70) and Eq.(71) lead one to the conclusions that the high temperature T_1 data and the d.c. conductivity data both measure the behavior of the correlation function at long times and that the low temperature T_1 data and the high frequency conductivity data both measure the short time behavior of the correlation function.

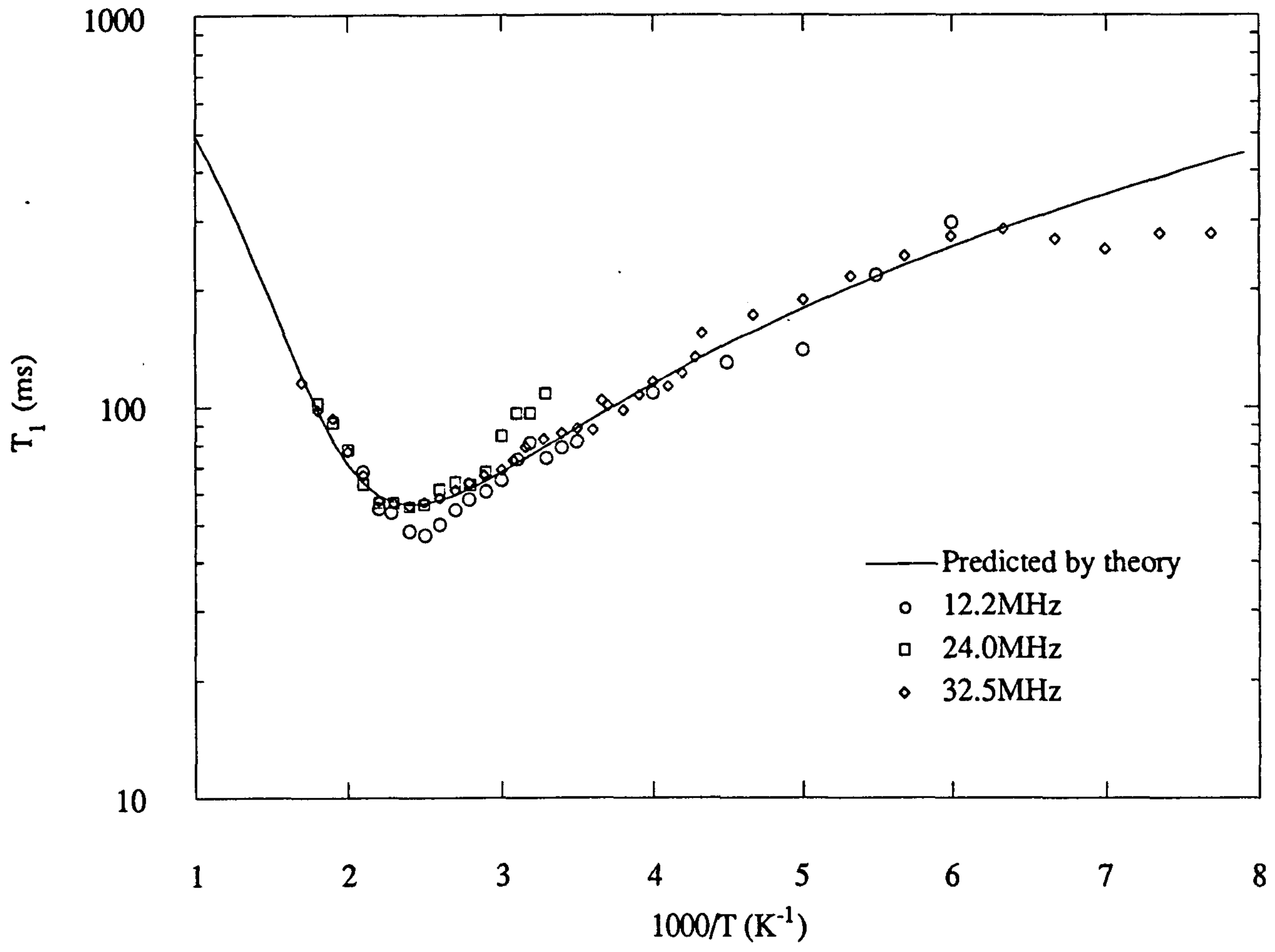

Figure 26. ^{11}B T_1 data for B_2O_3+0.7Li_2O+0.6LiCl glass with theoretical fit

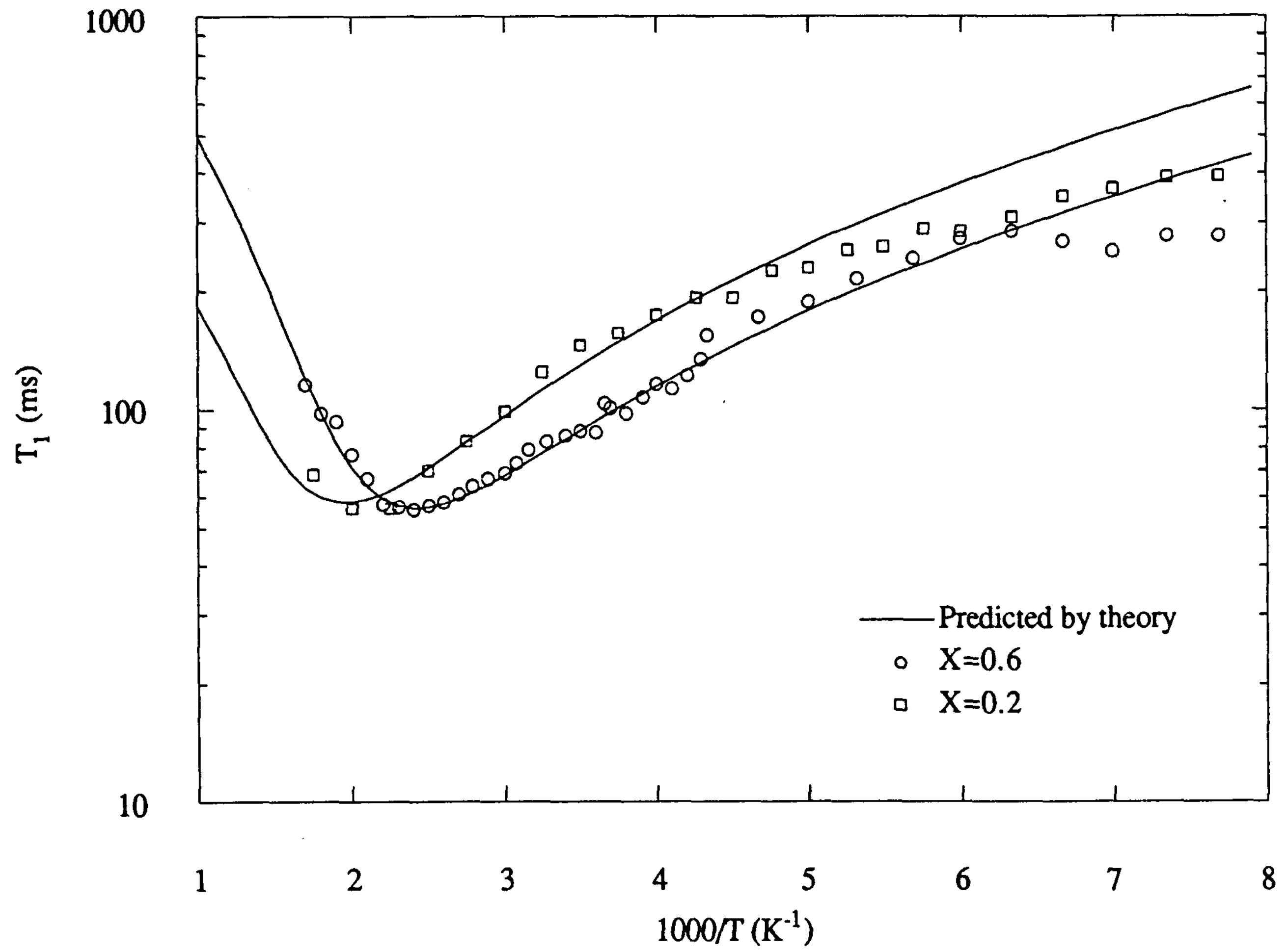

Figure 27. ^{11}B T_1 data for B_2O_3+0.7Li_2O+XLiCl glass for X = 0.2 and X = 0.6 with theoretical fit

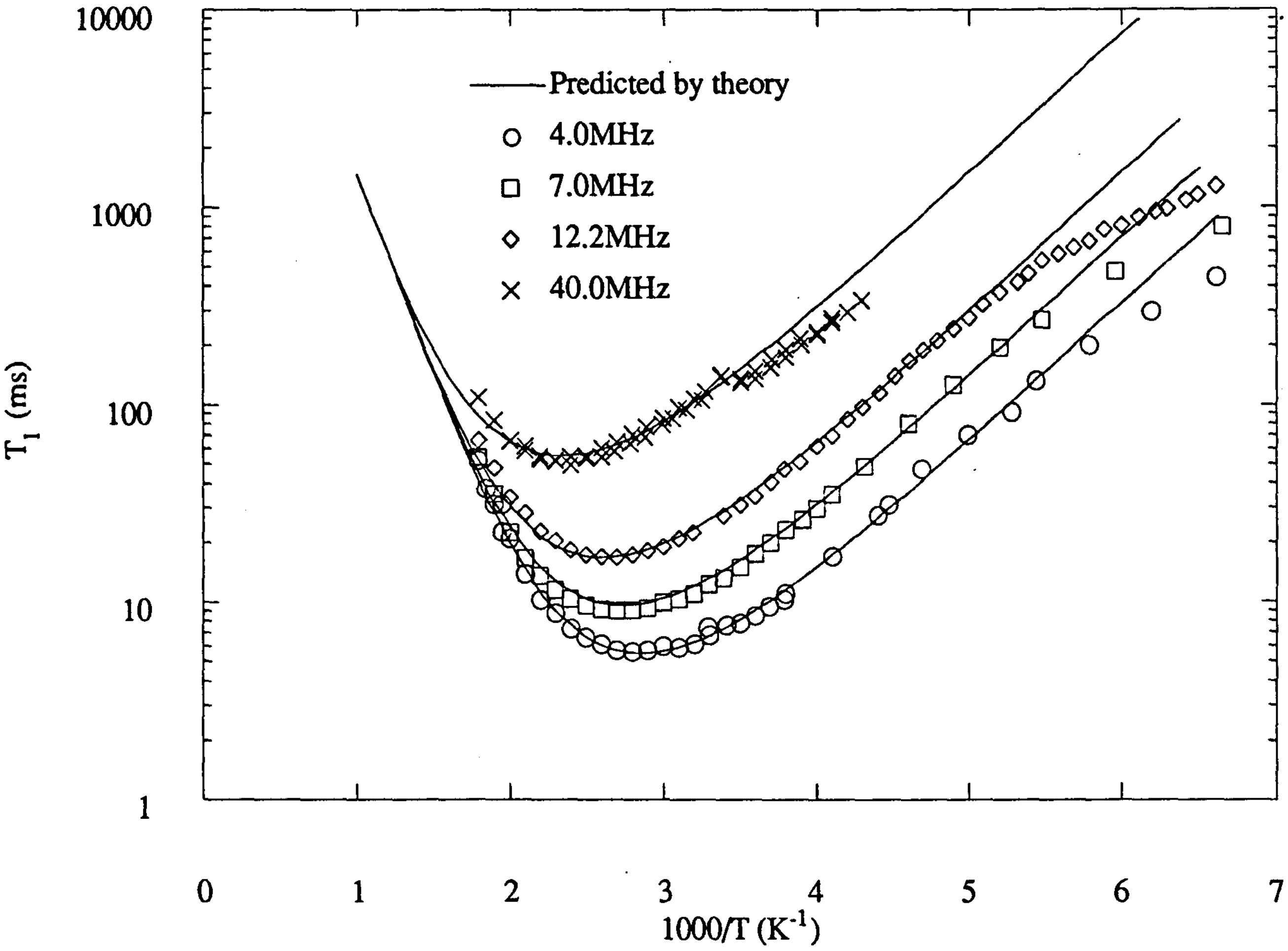

Figure 28. ^{7}Li T_1 data for 56% Li_2S 44% SiS_2 glass with theoretical fits using the KWW form of the correlation function

VI. SUMMARY AND CONCLUSIONS

The NMR spectra and T_1 measurements on both the stationary ^{11}B in the lithium chloroborate glass and on the mobile ^7Li in both the lithium chloroborate and lithium thiosilicate glasses has yielded much useful information about the static and dynamic properties of these two glassy fast ionic conductors.

The ^{11}B spectra (see Figures 12-14) for the B_2O_3+0.7Li_2O+XLiCl glasses indicates that the boron nuclei sit in two different sites. The narrow central line is due to the ^{11}B nuclei that are in the BO_4 sites where there is no EFG and therefore no electric quadrupole effects and no splitting of the line. The broader pattern consisting of the two side peaks is a result of the ^{11}B nuclei that sit in the BO_3 sites. In these sites, the magnitude of the EFG tenser is large and second order splitting of the central transition is seen. These side peaks are smaller since they are due to essentially the same number of boron nuclei but the pattern is spread over a much larger range of frequencies. If a baseline for these spectra could be determined, the ratio of BO_3 to BO_4 could then be found.

Nuclear spin lattice relaxation measurements of the ^{11}B nuclei show no dependence on the measuring frequency (see Figure 26). Because of this, the theory proposed by Rubinstein and Resing[38,39] which uses an adaptation of the Van Kronendonk[60] theory and uses a two phonon Raman process for the relaxation is favored. It seems reasonable that theories such as the BPP[34] (see Section II.C.3) theory should not work since they are designed for nuclei that exhibit diffusional motion and as it has been shown that the boron nuclei are fixed in their positions within the glass matrix and do not diffuse. The dependence of the minimum of T_1 on the concentration of the LiCl (see Figure 27) is evidence of some coupling between the ^{11}B relaxation and the lithium diffusional motion.

Spin lattice relaxation measurements of the ^7Li nuclei do show the frequency dependence that one expects from the nuclei that are free to diffuse through the glass matrix. Attempts to fit this data by using the BPP[34] theory fail, however a good fit can be obtained from using the KWW[35-37] form of the correlation function (see Section II.C.4). The X=0.6 and X=0.2 data can both be fit by using the same values of the parameters except for the value of τ_0 which decreases by a factor of three when X increases from 0.2 to 0.6 (see Table 7). There is some deviation of the data from the theory due to additional effects that occur at low temperatures and high fields.

The ^7Li nuclear spin lattice relaxation measurements from the 56% Li_2S+44% SiS_2 sample (see figure 28) also can not be fit by using the BPP[34] theory but by using the

KWW[35-37] form of the correlation function a good fit of the data is obtained. It is also shown that the a.c. conductivity data can also be fit well by also using the KWW[35-37] form of the correlation function but with different values of β (see Table 8). Since the measured values of β are different for the NMR and conductivity measurements ($\beta = 0.36$ and $\beta = 0.46$ respectively) it is believe that the stretched exponential is not caused by a simple distribution of activation energies but rather that $\beta < 1$ is due to a collective effect of the lithium motion. If β were due to a distribution of correlation functions then one would expect the same value of β for both of the measurements.

Much more work needs to be done on these glasses in order to gain a better understanding of the mechanisms at work. Future studies could include measuring the recovery time for a variety of samples with varying concentrations of alkali halides and alkali oxides of alkali thiosilicates to find the effects of these concentrations and to aid in the confirmation of the coupling between the mobile cations and the stationary nuclei. One could also find a fast ionic or super ionic glass where T_{1min} occurs at a low enough temperature compared to its glass temperature that enough data can be taken on the high temperature side. They could also include a study of the anomalies that occur at high frequencies and at low temperatures.

VII. ACKNOWLEDGMENTS

I wish to thank my adviser F. Borsa for not only teaching me science but more importantly how to do science. I also wish to thank D.R. Torgeson for all of the assistance he gave while I was taking the data for this thesis and to H. Patel and M. Tatsumisago for preparing the samples used.

Thanks also goes to my parents Don and Irene for their continued support in all that I do and to the other graduate students for helping me waste all those hours playing hundreds of dart games when I should have been working. I would also like to thank my undergraduate adviser Dr. Dale Olsen for giving me my first opportunity to do research which sparked my interest in pursuing graduate school.

This work was performed at Ames Laboratory under contract no. W-7405-eng-82 with the U.S. Department of Energy. The United States government has assigned the DOE Report number IS-T 1525 to this thesis.

VIII. BIBLIOGRAPHY

[1]C.A. Angell, Solid State Ionics **18-19**, 72 (1985).

[2]S.W. Martin, Mater. Chem. Phys. **23**, 225 (1989).

[3]J. Krogh-Moe, Phys. Chem. Glasses **6**, 46 (1965).

[4]J. Krogh-Moe, Phys. Chem. Glasses **3**, 101 (1962).

[5]J. Krogh-Moe, Acta Cryst. **13**, 889 (1960).

[6]J. Krogh-Moe, Acta Cryst. **15**, 190 (1962).

[7]W.H. Zachariasen and H.A. Plettinger, Acta Cryst. **16**, 376 (1968).

[8]P.J. Bray and J.G. O'Keefe, Phys. Chem. Glasses **4**, 37 (1963).

[9]S. Greenblatt and P.J. Bray, Phys. Chem. Glasses **8**, 213 (1967).

[10]C. Rhee and P.J. Bray, J. Chem. Phys. **56**, 2476 (1972).

[11]G.E. Jellison, Jr. and P.J. Bray, J. Non-Cryst. Solids **29**, 187 (1978).

[12]P.J. Bray, S.A. Feller, G.E. Jellison, Jr. and Y.H. Yun, J. Non-Cryst. Solids **38**, 93 (1980).

[13]P.J. Bray, J. Non-Cryst. Solids **73**, 19 (1985).

[14]P.J. Bray, J. Non-Cryst. Solids **75**, 29 (1985).

[15]K.S. Kim and P.J. Bray, J. Nonmetals **2**, 95 (1974).

[16]H.Eckert, J.H. Kennedy, A. Pradel and M. Ribes, J. Non-Cryst. Solids **113**, 287 (1989).

[17]E. Lippmaa, M. Magi, A. Samoson, G. Engelhardt and A.R. Grimmer, J. Am. Chem. Soc. **102**, 4889 (1990).

[18]H. Eckert, Z. Zhang and J.H. Kennedy, J. Non-Cryst. Solids **107**, 271 (1989).

[19]M. Tenhover, R.D. Henredson, T.E. Hammond and G.A. Shreve, Solid State Commun. **65**, 1517 (1988).

[20]K. Singh and J.S. Ratnam, Solid State Ionics **31**, 221 (1988).

[21]A. Levasseur, J.C. Brethous, J.M. Réau and P. Hagenmuller, Mat. Res. Bull. **14**, 921 (1979).

[22]H.L. Tuller, D.P. Button and D.R. Uhlmann, J. Non-Cryst. Solids **40**, 93 (1980).

[23]A. Levasseur, J.C. Brethous, M. Kbala and P. Hagenmuller, Solid State Ionics **5**, 651 (1981).

[24]D.P. Button, L.S. Mason,H.L. Tuller and D.R. Uhlmann, Solid State Ionics **9-10**, 585 (1983).

[25]A. Pradel and M. Ribes, Solid State Ionics **18-19**, 351 (1986).

[26] S. Sahami, S.W. Shea and J.H. Kennedy, J. Electrochem. Soc. **132**, 935 (1985).

[27] J.H. Kennedy and Z. Zhang, J. Electrochem. Soc. **135**, 859 (1988).

[28] J.H. Kennedy and Y. Yang, J. Electrochem. Soc. **133**, 2437 (1986).

[29] V.K. Deshponde, A Pradel and M. Ribes, Solid State Ionics **28-30**, 756 (1988).

[30] P.B. Macedo, C.T. Moynihan and R. Bose, Phys Chem. Glasses **13**, 171 (1972).

[31] P. Provenzano, L.P. Boesch, V. Volterra, C.T. Moynihan and P.B. Macedo, J. Am. Ceram. Soc. **55**, 492 (1972).

[32] K.L. Ngai, J.N. Mundy, H.G. Jain, O. Kanert and G. Balzer-Jollenbeck, Phys. Rev. **39**, 6169 (1988).

[33] E.L. Pollock and B.J. Adler, Phys. Rev. Lett. **46**, 950 (1981).

[34] N. Bloembergen, E.M. Purcell and R.V. Pound, Phys. Rev. **73**, 679 (1948).

[35] G. Williams and D.C. Watts, Trans. Faraday Soc. **66**, 80 (1970).

[36] R. Kohlrausch, Pogg. Ann. Phys. **92**, 56 (1854).

[37] R. Kohlrausch, Pogg. Ann. Phys. **92**, 179 (1854).

[38] M. Rubenstein, H.A. Resing, T.L. Reinecke and K.L. Ngai, Phys. Rev. Lett. **34**, 1444 (1975).

[39] M. Rubinstein and H.A. Resing, Phys. Rev. B **13**, 959 (1976).

[40] A. Avogadro, S. Manzini and M. Villa, Phys. Rev. Lett. **44**, 256 (1980).

[41] A. Avogadro, F. Tabak, M. Corti and F. Borsa, Phys. Rev. B **41**, 6137 (1990).

[42] R.C. Weast, *Handbook of Chemistry and Physics* (CRC Press, Boca Raton, 1982).

[43] Personal communication, F. Borsa.

[44] F. Bloch, Phys. Rev. **70**, 460 (1947).

[45] E. Fukushima and S.B.W. Roeder, *Experimental Pulse NMR; A Nuts and Bolts Approach* (Addison-Wesley, Reading, 1981).

[46] J.H. VanVleck, Phys Rev. **74**, 1168 (1948).

[47] A. Abragam, *The Principles of Nuclear Magnetism* (Oxford, London, 1961).

[48] G.C. Carter, L.H. Bennett and D.J. Kahan, *Metallic Shifts in NMR; A Review of the Theory and Comprehensive Critical Data Compilation of Metallic Materials* (Pergamon Press, Oxford, 1977).

[49] R.B. Creel, Ph.D. Thesis, Iowa State University, 1969 (Unpublished).

[50] E.R. Andrew and D.P. Turnstall, Proc. Phys. Soc. **78**, 1 (1961).

[51] M.I. Gordon and M.J.R. Hoch, J. Phys. C: Solid State Phys. **11**, 783 (1978).

[52] F. Borsa, in *Local Properties at Phase Transitions*, edited by K.A. Muller and A, Rigamonti (Editrice Compositori, Bologna, 1975).

[53] M. Dishon, G.H. Weiss and J.T. Bendler, J. Res. Nat. Bureau Stand. **90**, 27 (1985).

[54] D.R. Torgeson, unpublished.

[55] D.J. Adduci and B.C. Gerstein, Rev. Sci. Instrum. **50**, 1403 (1979).

[56] D.R. Torgeson and D.J. Adduci, unpublished.
D.J Adduci, P.A. Hornung and D.R Torgeson, Rev. Sci. Instrum. **47**, 1503 (1976).

[57] D. Jensen, unpublished.

[58] R.G Leconder and D.R. Torgeson, unpublished.

[59] H. Grüne, H. Meierkord, W. Müller-Warmuth, P. zum Hebel, B. Krebs and M. Wulff, Ber. Bunsenges. Phys. Chem. **93**, 1313 (1989).

[60] J. Van Kranendonk, Physica (Utr.) **20**, 781 (1954).

[61] *VAX-11 FORTRAN Language Reference Manual* (Digital Equipment Corporation, 1980).

[62] M. Abramowitz and I.A. Stegun, *Handbook of Mathematical Functions, AMS 55* (Government Printing Office, Washington, DC, 1970).

[63] see for example P.R. Bevington, *Data Reduction and Error Analysis for the Physical Sciences* (McGraw-Hill, New York, 1969).

IX. APPENDIX A: FITTING DATA WITH THE KWW THEORY

A. Numerical Evaluation of Integrals

In this section some of the difficulties associated with evaluating the integrals that result when the KWW form of the correlation function is used will be examined. The two integrals are

$$Q_\alpha(z) = \int_0^\infty \cos(zu)\, e^{-u^\alpha}\, du \qquad (72)$$

and

$$V_\alpha(z) = \int_0^\infty \sin(zu)\, e^{-u^\alpha}\, du \qquad (73)$$

If these are substituted into the theory for a.c. conductivity, Eq.(63) becomes

$$\sigma'(\omega) = B\,\frac{\omega}{z}\,\frac{Q_\alpha(z)}{\left[Q_\alpha(z)\right]^2 + \left[V_\alpha(z)\right]^2} \qquad (74)$$

where $u = \frac{t}{\tau_c}$, $z = \omega\tau_c$ and $B = \frac{\varepsilon_0}{M_\infty}$.

Using the same definitions of u and z, Eq.(48) for the nuclear spin lattice relaxation time becomes

$$\frac{1}{T_1} = A\,\frac{z}{\omega}\left[Q_\alpha(z) + Q_\alpha(2z)\right]. \qquad (75)$$

A list of values for $Q_\alpha(z)$ and $V_\alpha(z)$ are given by Dishon, Weiss and Bendler[53] for a few values of α and values of z ranging from 0.001 to 2500. Note that the definitions of $Q_\alpha(z)$ and $V_\alpha(z)$ given in the reference differ from Eq.(72) and Eq.(73) by a factor of π. The values of α used in the reference range from 0.02 to 2 but in the range where $\alpha = 0.36$ or $\alpha = 0.46$, α increases by steps of 0.1 which is too corse for what is needed here therefore the lists of values for these integrals must be generated. Here the emphasis will be on evaluating $Q_\alpha(z)$ but $V_\alpha(z)$ poses the same difficulties and these difficulties have similar solutions.

Attempts at evaluating $Q_\alpha(z)$ using standard numeric integration techniques such as the trapezoid rule and Simpson's rule fail due to two factors: the stretched exponential term converges to zero very slowly and the cosine term oscillates very rapidly. If $z = 10^7$ and $\alpha = 0.1$ and 1000 steps are taken within each oscillation of the cosine term, the result is approximately 10^{14} steps, at 1000 steps per second it would take about 3000 years to evaluate $Q_\alpha(z)$ once.

With the direct methods being hopeless, a change of variable is tried. The most useful is something of the form $u = \tan(\theta)$ which leads to

$$Q_\alpha(z) = \int_0^{\pi/2} e^{-\tan^\alpha(\theta)} \frac{\cos(z \tan\theta)}{\cos^2\theta} \quad . \qquad (76)$$

This has the problem that as $\theta \rightarrow \frac{\pi}{2}$, $\tan(\theta) \rightarrow \infty$ and the frequency of oscillation of $\cos(\tan(\theta))$ also approaches infinity, however, if z is small enough or α is large enough then the stretched exponential term becomes nearly zero before the oscillations get too fast and therefore the integral can be accurately determined by standard techniques.

In order to evaluate $Q_\alpha(z)$ for large z or small α another technique must be used. If a Taylor series of the integrand is performed, the result is[53]

$$Q_\alpha(z) = \sum_{n=1}^{\infty} (-1)^{n+1} \frac{\Gamma(1+n\alpha)}{n!\, z^{1+n\alpha}} \sin\left(\frac{n\pi\alpha}{2}\right) \quad . \qquad (77)$$

This series converges for $\alpha < 1$ but works best when α is small or z is large and can be used whenever Eq.(76) fails.

There are certain difficulties associated with the evaluation of Eq.(78). If the middle term of Eq.(77) is examined, it is seen that it involves both a Γ function and a factorial function neither of which exist is most standard computer languages and therefore routines must be written to calculate them. Another problem is that the both the Γ and factorial functions grow very rapidly but for $\alpha < 1$ the factorial is larger for a given n. In standard FORTRAN[61] if n! were to represented as an integer the largest value of n that could be used is $n = 12$ since integers can only go up to about 2.1×10^9. If a REAL*4 variable is used it is possible to go as large as n! = 1.7×10^{38} giving 33 terms of the series. By going to a REAL*8 variable with the G_FLOATING compilation option, numbers as large as 9×10^{307} can be obtained which would allow the use of 170 terms which in most cases is enough. If however more terms are needed, a REAL*16 variable on a machine with the extended floating-point option could be used and numbers as large as 5.9×10^{4931} can be obtained which would allow the use of almost 1500 terms. It should be noted that if the higher precision variables are used the calculations will be performed much more slowly therefore one should not use precision greater than that which is required for the data to be fit.

Calculation of the factorial is straight forward so it will not discussed here but the Γ function will be examined. Several expansions of the Γ function exist and have been tried; the best one seems to be Euler's Infinite Product:[62]

$$\frac{1}{\Gamma(x)} = xe^{\gamma x} \prod_{n=1}^{\infty} \left[\left(1 + \frac{x}{n}\right) e^{-x/n} \right] \tag{78}$$

where γ is Euler's constant. This product converges fairly rapidly and therefore $\Gamma(x) = \Gamma(1+n\alpha)$ can be calculated quickly. Another expansion that works quicker but has less accuracy at small values of x is Sterling's Formula which states

$$\Gamma(z) = e^{-x}\, x^{x-\frac{1}{2}} (2\pi)^{\frac{1}{2}} \left[1 + \frac{1}{12x} + \frac{1}{288x^2} - \frac{139}{51840x^3} - \frac{571}{2488320x^4} + \ldots \right]. \tag{79}$$

Another method that works very quickly is instead of calculating the Γ and factorial functions, calculating the natural logarithm of them and substituting into Eq.(77)

$$\frac{\Gamma(z)}{n!\, z^{1+n\alpha}} = \exp\{\ln[\Gamma(1+n\alpha)] - \ln(n!) - (1+n\alpha)\ln(z)\} \tag{80}$$

The natural logarithm of the Γ function can be easily found from[62]

$$\ln[\Gamma(x)] = (x - \tfrac{1}{2})\ln(x) - x + \tfrac{1}{2}\ln(2\pi) + \frac{1}{12x} - \frac{1}{360x^3} + \frac{1}{1260x^5} - \frac{1}{1680x^7} + \ldots \tag{81}$$

and the factorial becomes

$$\ln(n!) = \ln(1) + \ln(2) + \ln(3) + \cdots + \ln(n) \tag{82}$$

A simple FORTRAN program that uses the above method to calculate $Q_\alpha(z)$ for $\alpha = 0.36$ and $0.1 \leq z \leq 10000000$ is shown in Figure 29 with the output is shown in Table 9.

B. Fitting The Data

Fitting a theoretical curve to experimental data poses special problems when there is no analytic form for the theory. When the theory can be expressed as a function of the dependent and independent variables such as the BPP theory, computer fitting routines can be employed to give a best fit of the data.[63] When the theory can not be expressed as a function as is the case with the KWW theory, some other techniques must be used.

The method used to fit the data shown in Figures 24, 25 and 28 were fit by adjusting the various parameters until the fit looked good. Although this is not as precise as a least squares fit, it is good enough for the purposes of this work. A method for doing these fits is described below.

First a table of numbers consisting of z vs. $Q_\alpha(z)$ and $Q_\alpha(2z)$ for each value of β ($= \alpha$) that will be needed must be generated. Alternately a table of numbers consisting of z vs. $[Q_\alpha(z)+Q_\alpha(2z)]$ could also be generated. Next estimates of the values of E_a, τ_0 and β need to be made by using Eq.(65) through Eq.(67); assume that ω is a constant. From these and the table of z vs. $[Q_\alpha(z)+Q_\alpha(2z)]$ a new table consisting of

$$T_1 = \frac{\omega}{Az}[Q_\alpha(z) + Q_\alpha(2z)]^{-1} \tag{83}$$

and

$$\frac{1000}{T} = \frac{1000k_B}{E_a}\ln\left(\frac{z}{\omega\tau_0}\right) \tag{84}$$

needs to be created. The data to be fit and the generated values of T_1 vs. $\frac{1000}{T}$ is then plotted to see how good the fit is. In all probability, some adjustments will need to be made.

The first variable of concern is the activation energy E_a. This can be determined more accurately by matching the slope of the data on the high temperature side of the minimum to the slope of the theoretical curve in the same region. The slope is also very weakly dependent on τ_0 but that can be ignored for now.

Next the value of β needs to be determined. This is done by matching the slopes on the low temperature side of the respective minima. Once these have been done the last two variables can be fit.

Fitting these final variables is made simpler since they are independent of each other. As can seen, τ_0 does not appear in Eq.(84) which adjusts the value of T_1 and A does not appear in Eq.(85) for $\frac{1000}{T}$. These two parameters are adjusted to bring the curve and the data together. This is most easily done if only at the relative placements of the minima is examined and the rest of the data ignored

Once the minima have been aligned, the values of E_a and β can be adjusted to make the fit better. Several items need to be noted here. Small changes in E_a will need to be compensated for by large changes in τ_0 since τ_0 appears as a logarithm but these will not affect the value of A chosen. If the value of β needs to be adjusted then both A and τ_0 will need to be adjusted assuming the E_a has already been determined.

This scheme works well if data exists on both the high and low temperature sides of the minimum as in Figure 28. If there is data only on the low temperature side as in Figures 24 and 25 then the values of E_a and β are much more difficult to determine. For these cases the slope on the low temperature side of the minimum should be fit and then the value of $\beta \times E_a$ can been determined and can be held constant, an increase in β by some factor must be compensated for by a decrease in E_a by the same factor. After trying several different combinations of E_a and β a best fit can be determined.

```
      INTEGER M,N
      REAL*8 P2,TP,PA,GAMMA,FACT,BETA,Z,Q,ONA,SIGMA,D
      TP=6.2831853071795864769252867
      P2=1.5707963267948966192313322
      BETA=0.36
      OPEN(1,NAME='ZQ36.OUT',TYPE='NEW',FORM='FORMATTED')
      WRITE(1,*)'BETA=',BETA
      WRITE(1,*)' Z                         Q'
C     loop to generate 81 values of z from 0.1 to 10000000
      DO 5 M=0,80
         Z=10**(M/10D+00-1D+00)
C        loop to calculate terms in series expansion of Q
         DO 10 N=1,1000
            ONA=1D+00+N*BETA
C           expansion of ln(gamma(ona))
            GAMMA=(ONA-0.5D+00)*LOG(ONA)-ONA+0.5D+00*LOG(TP)
            GAMMA=GAMMA+1/(12*ONA)-1/(360*ONA**3)
            GAMMA=GAMMA+1/(1260*ONA**5)-1/(1680*ONA**7)
C           ln(n!) D is a real variable equal to integer N
            D=N
            FACT=FACT+LOG(D)
C           PA = gamma(ona)/(n!*Z**ona)
            PA=EXP(GAMMA-FACT-ONA*LOG(Z))
            Q=Q+((-1)**(N-1))*PA*SIN(N*P2*BETA)
10       CONTINUE
         WRITE(1,*)Z,Q
         Q=0.0D+00
         FACT=0.0D+00
5     CONTINUE
      CLOSE(1)
      STOP
      END
```

Figure 29. FORTRAN program used to calculate values for $Q_\alpha(z)$

Table 9. Output of FORTRAN program shown in Figure 29

```
BETA=0.360000000000000
Z                           Q
0.100000000000000           1.51555658049582
0.125892541179417           1.28963702266172
0.158489319246111           1.08573865318178
0.199526231496888           0.904852863389756
0.251188643150958           0.746908400446246
0.316227766016838           0.610996735022685
0.398107170553497           0.495606532462116
0.501187233627272           0.398842632851778
0.630957344480193           0.318614217568827
0.794328234724281           0.252784968729009
1.00000000000000            0.199284247092983
1.25892541179417            0.156182465919178
1.58489319246111            0.121736148494077
1.99526231496888            9.440903398338436E-002
2.51188643150958            7.287548638571745E-002
3.16227766016838            5.601176307240943E-002
3.98107170553497            4.287972370011712E-002
5.01187233627272            3.270652392937251E-002
6.30957344480193            2.486287488589160E-002
7.94328234724281            1.884162757697313E-002
10.0000000000000            1.423778535899580E-002
12.5892541179417            1.073055270289343E-002
15.8489319246111            8.067675362555374E-003
19.9526231496888            6.052089832838893E-003
25.1188643150958            4.530752331367547E-003
31.6227766016838            3.385435643853686E-003
39.8107170553497            2.525246167384189E-003
50.1187233627273            1.880607739318986E-003
63.0957344480193            1.398471648895696E-003
79.4328234724282            1.038535226752635E-003
```

Table 9. Continued

100.000000000000	7.702788875178108E-004
125.892541179417	5.706597762130112E-004
158.489319246111	4.223270237545101E-004
199.526231496888	3.122478580956982E-004
251.188643150958	2.306549363404730E-004
316.227766016838	1.702431818083645E-004
398.107170553497	1.255593044359533E-004
501.187233627272	9.253936126486408E-005
630.957344480193	6.815953763933226E-005
794.328234724282	5.017316522947900E-005
1000.00000000000	3.691318291345140E-005
1258.92541179417	2.714409641110673E-005
1584.89319246111	1.995126548044135E-005
1995.26231496888	1.465826439662336E-005
2511.88643150958	1.076530424743122E-005
3162.27766016838	7.903421768617558E-006
3981.07170553497	5.800447042048725E-006
5011.87233627273	4.255754864633680E-006
6309.57344480193	3.121555334594919E-006
7943.28234724282	2.289045338753856E-006
10000.0000000000	1.678168376568317E-006
12589.2541179417	1.230049539891916E-006
15848.9319246111	9.014115192532924E-007
19952.6231496888	6.604560695727875E-007
25118.8643150958	4.838285014772033E-007
31622.7766016838	3.543818606726819E-007
39810.7170553497	2.595311070778580E-007
50118.7233627273	1.900422665366125E-007
63095.7344480193	1.391420453354682E-007
79432.8234724282	1.018633966944672E-007
100000.000000000	7.456471624686274E-008
125892.541179417	5.457673842072236E-008

Table 9. Continued

158489.319246111	3.994330945591368E-008
199526.231496888	2.923114150450211E-008
251188.643150958	2.139023395649970E-008
316227.766016838	1.565149650095400E-008
398107.170553497	1.145167776589924E-008
501187.233627271	8.378329622162759E-009
630957.344480194	6.129468575059675E-009
794328.234724282	4.484015305020908E-009
1000000.00000000	3.280136475165542E-009
1258925.41179417	2.399378989835212E-009
1584893.19246111	1.755049314899316E-009
1995262.31496888	1.283703252369729E-009
2511886.43150958	9.389144215554803E-010
3162277.66016838	6.867118457267041E-010
3981071.70553497	5.022399450444652E-010
5011872.33627271	3.673136651158145E-010
6309573.44480194	2.686290083793017E-010
7943282.34724282	1.964533854361147E-010
10000000.0000000	1.436672054071183E-010